EUROPEAN ORGANIZATION FOR NUCLEAR RESEARCH

CERN-EP/82-210
15 December 1982

NEUTRINO AND ANTINEUTRINO CHARGED-CURRENT INCLUSIVE SCATTERING IN IRON IN THE ENERGY RANGE $20 < E_\nu < 300$ GeV

H. Abramowicz[1], J.G.H. de Groot, J. Knobloch, J. May, P. Palazzi,
A. Para[1], F. Ranjard, A. Savoy-Navarro[2], D. Schlatter, J. Steinberger,
H. Taureg, W. von Rüden, H. Wahl and J. Wotschack

CERN, Geneva, Switzerland

P. Buchholz, F. Eisele, H.P. Klasen, K. Kleinknecht, H. Lierl, D. Pollmann, B. Pszola,
B. Renk and H.J. Willutzki

Institut für Physik* der Universität Dortmund, Fed. Rep. Germany

F. Dydak, T. Flottmann, C. Geweniger, J. Królikowski[1] and K. Tittel

Institut für Hochenergiephysik* der Universität Heidelberg, Fed. Rep. Germany

P. Bloch, B. Devaux, C. Guyot, J.P. Merlo, B. Peyaud, J. Rander,
J. Rothberg[3] and R. Turlay

DPhPE, CEN-Saclay, France

J.T. He, T.Z. Ruan and W.M. Wu

Institute of High-Energy Physics, Beijing, China

(Submitted to Zeitschrift für Physik C)

---

*) Supported by the Bundesministerium für Forschung und Technologie, Bonn, Fed. Rep. Germany.

1 On leave from the Institute of Experimental Physics, Warsaw University, Poland.
2 On leave from the DPhPE, CEN-Saclay, France.
3 On leave from the University of Washington, Seattle, USA.

ABSTRACT

Inclusive charged-current interactions of high-energy neutrinos and anti-neutrinos have been studied with high statistics in a counter experiment at the CERN Super Proton Synchrotron. The energy dependence of the total cross-sections, the longitudinal structure function, and the nucleon structure functions F_2, xF_3, and $\bar{q}^{\bar{\nu}}$ are determined from these data. The analysis of the Q^2-dependence of the structure functions is used to test quantum chromodynamics, to determine the scale parameter Λ and the gluon distribution in the nucleon.

1. INTRODUCTION

The inclusive scattering of neutrinos and antineutrinos is of interest chiefly as a means of studying the structure of the nucleon and the strong interactions. The Callan-Gross relation [1], the Gross-Llewellyn Smith [2] sum rule, and the comparison of neutrino and charged lepton structure functions, permit tests of the quark parton model. The structure functions themselves show us how the quarks and gluons share the nucleon momentum, in particular, the small deviation from scaling permits a quantitative confrontation of quantum chromodynamics (QCD) with experiment.

We report here experimental results which are more extensive and precise than our previously published results [3-5]. In this work we were largely motivated by the interest in improving the comparison of the structure functions with QCD predictions. The results are based on the analysis of data obtained in 200 GeV neutrino and antineutrino narrow-band beams, in a 300 GeV narrow-band neutrino beam, and also in wide-band beams of both polarities. In total, we report here on 130,000 neutrino and 180,000 antineutrino charged-current events, after event selection, which can be compared with 23,000 and 6,200 events, respectively, in the previous publication [3].

Partial results based on the same data have already been published. These include the measurement of the longitudinal structure function [6], a limit on right-handed currents [7], the determination of the gluon distribution in the nucleon [8], and the comparison of the measured structure functions with QCD and non-asymptotically free theories of the strong interaction [9].

2. PHENOMENOLOGY

The kinematic quantities for inclusive charged-current scattering are defined in the usual way:

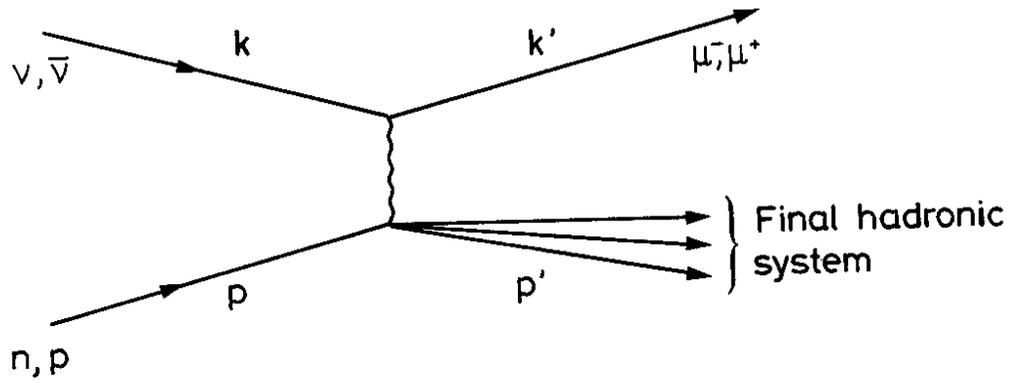

$Q^2 = -(k - k')^2$

$\nu = (k - k') \cdot p/m_N$, where m_N = nucleon mass

$x = Q^2/2m_N\nu$

$y = m_N\nu/k \cdot p \simeq E_h/E_\nu$, where E_ν and E_h are the kinetic energy of the neutrino and of the hadron system in the laboratory system, respectively.

Assuming the standard V - A theory of the weak interactions, the neutrino and antineutrino charged-current cross-sections can each be written in terms of three structure functions:

$$\frac{d^2\sigma^{\nu,\bar{\nu}}}{dxdy} = \frac{G^2 m_N E_\nu}{\pi} \frac{1}{(1 + Q^2/m_W^2)^2} \left\{ \left[1 - y - \frac{m_N xy}{2E_\nu} \right] F_2^{\nu,\bar{\nu}}(x,Q^2) \right. \tag{1}$$

$$\left. + \frac{y^2}{2} 2xF_1^{\nu,\bar{\nu}}(x,Q^2) \pm \left[y - \frac{y^2}{2} \right] xF_3^{\nu,\bar{\nu}}(x,Q^2) \right\} .$$

The propagator term $(1 + Q^2/m_W^2)^{-2}$ is a small correction. With a vector boson mass of $m_W \simeq 80$ GeV, as predicted in the Weinberg-Salam theory, and using the present experimental value for the electroweak angle, the correction of the cross-section is about 10% at the highest Q^2 of this experiment. It will be dropped in all formulae which follow.

In the quark parton model the structure functions are written in terms of the quark and antiquark momentum distributions in the nucleon. For isoscalar nuclei we have

$$2xF_1^{\nu}(x,Q^2) = 2xF_1^{\bar{\nu}}(x,Q^2) = q(x,Q^2) + \bar{q}(x,Q^2) \tag{2}$$

= total momentum distribution of quarks and antiquarks.

$$F_2^{\nu,\bar{\nu}}(x,Q^2) = 2xF_1(x,Q^2) + F_L(x,Q^2) \tag{3}$$

$$xF_3^{\nu,\bar{\nu}}(x,Q^2) = q(x,Q^2) - \bar{q}(x,Q^2) \pm 2x\left[s(x,Q^2) - c(x,Q^2)\right] \tag{4}$$

$$xF_3(x,Q^2) = \frac{1}{2}(xF_3^{\nu} + xF_3^{\bar{\nu}}) = q(x,Q^2) - \bar{q}(x,Q^2) \ . \tag{5}$$

Here xF_3 is the momentum distribution of the valence quarks inside the nucleon, $F_L = F_2 - 2xF_1$ is the longitudinal structure function, and q and $\bar{q}$ are the sum of quark and antiquark momentum distributions, respectively:

$$q = x(u + d + s + c)$$

$$\bar{q} = x(\bar{u} + \bar{d} + \bar{s} + \bar{c}) \ ;$$

u, d, s, and c are the up, down, strange, and charmed quark distribution as seen by the weak charged current.

If the transverse momentum of the quarks with respect to the nucleon momentum can be neglected, F_L is zero and the Callan-Gross relation [1] $F_2 = 2xF_1$ is valid. If F_L can be neglected, the neutrino and antineutrino cross-sections then have the simple form:

$$\frac{d^2\sigma^{\nu}}{dxdy} \sim \frac{G^2 m_N E_\nu}{\pi} \left\{ q + x(s-c) + (1-y)^2 \left[\bar{q} - x(\bar{s}-\bar{c})\right] \right\} \ , \tag{6}$$

$$\frac{d^2\sigma^{\bar{\nu}}}{dxdy} \sim \frac{G^2 m_N E_\nu}{\pi} \left\{ \bar{q} + x(\bar{s}-\bar{c}) + (1-y)^2 \left[q - x(s-c)\right] \right\} \ . \tag{7}$$

The expressions (3) to (7) are valid up to terms $\sim Q^2/\nu^2$ which have been dropped for the sake of simplicity. The general formulae which have been used in the analysis are given in the Appendix. A combined analysis of neutrino and antineutrino differential cross-sections allows the separate measurement of the valence and the sea-quark distributions, as will be shown in Section 4. This is a unique feature of neutrino experiments and is due to the V - A structure of charged-current weak interactions.

3. EXPERIMENTAL PROCEDURE

3.1 Apparatus

The detector has been described elsewhere [10]. It consists of 19 toroidally magnetized iron modules, each composed of circular plates 3.75 m in diameter, with a total iron thickness of 75 cm per module, corresponding to a mass of 65 t. These modules serve simultaneously as neutrino target, hadron-shower calorimeter, and muon-spectrometer magnet. Scintillator sheets are sandwiched between the iron plates, to sample the hadron-shower energy and to trigger the detector. Between modules, drift chambers are inserted, each with three wire planes inclined at 60° to each other. The first seven modules have scintillator planes every five centimetres of iron, the next eight have them every fifteen centimetres; the last four modules serve as muon analysers only and are equipped with a single plane of scintillators for triggering purposes (see Fig. 1).

The hadron-energy response and the resolution of the detector have been measured by putting three modules into a hadron beam [11]. The resolution is approximately equal to $\Delta E/E \simeq 0.7/\sqrt{E}$ for modules with 5 cm sampling, and $1.35/\sqrt{E}$ for 15 cm sampling. The scintillator and phototube responses are continuously monitored by means of cosmic-ray muons which are recorded between bursts.

The drift-chamber resolution, including the uncertainty in the wire positions, is about 1 mm. However, the muon momentum error is dominated by multiple scattering in the iron; for the data reported here it is, on the average, $\Delta p_\mu/p_\mu \simeq 9\%$. We note that the sign of the magnetic field is chosen such that the muons are focused towards the axis, and in general, owing to the large diameter and high density of the detector, the muons are trapped and leave the apparatus only through the end. As a consequence the muon acceptance for charged-current events is nearly one and uniform except for muons with momenta below $\sim$ 5 GeV, which do not traverse a sufficient number of drift chambers.

The fiducial mass of the detector is about 600 t, which gives rise to large event rates in intense neutrino beams. The rate of data taking is limited by the

conversion time of the pulse-height circuits of $\sim$ 2.5 μs. Pulse-height and drift-chamber circuits feed into fast buffers, 40 events deep, so that several events may be accepted even within the short 23 μs spill of narrow-band beams, and up to 40 events may be accepted within the millisecond spill of the wide-band beams.

The central area of the detector, where the magnet coils pass through, is not fully covered by scintillators. Furthermore, an area 30 cm in diameter (0.6% of the total area) is not magnetized, although it is filled with material of approximately the density of the iron. To ensure full shower containment and good muon-momentum measurement, events which originate in a lozenge-shaped region (as shown in Fig. 2) are excluded from the analysis. The centre of the neutrino beam is directed $\sim$ 45 cm below the centre of the modules so that we lose only a small fraction of all events with this cut and keep especially the highest energy neutrinos, which are in the beam centre.

The unique feature of this detector is the combination of calorimeter and muon spectrometer in one high-density unit, resulting in excellent muon acceptance. The hadron shower containment is complete in the fiducial region of about 600 t. These properties, combined with the ability to record large event numbers in intense neutrino beams, make this detector uniquely suitable for the systematic and precise measurement of inclusive neutrino cross-sections.

3.2 Neutrino beams

The data were obtained in five different beams. Some of the characteristics of the exposures are given in Table 1.

The neutrino fluxes corresponding to these exposures are shown in Figs. 3a and 3b. The energy dependence of the narrow-band beam spectra are determined by the geometrical properties of the hadron beams and by the kaon-to-pion ratios, which were measured periodically with a differential Cherenkov counter in front of the decay tunnel. The K/π ratios were found to be the following:

a) 200 GeV ν (400 GeV/c p) $K^+/\pi^+ = 0.146 \pm 0.005$

b) 200 GeV $\bar{\nu}$ (400 GeV/c p) $K^-/\pi^- = 0.049 \pm 0.002$

c) 200 GeV $\bar{\nu}$ (450 GeV/c p) $K^-/\pi^- = 0.056 \pm 0.002$

d) 300 GeV ν (400 GeV/c p) $K^+/\pi^+ = 0.24 \pm 0.01$.

The wide-band beam spectra are not measured externally but are derived from the observed charged-current event rates and the total neutrino cross-sections as measured in the narrow-band beams. In the present work, the wide-band beam data are used specifically to determine the antiquark structure function (Section 4.2.3), where the large statistics obtained in the wide-band beam outweigh the disadvantage that the spectrum is not determined independently.

3.3 Data selection and corrections

3.3.1 Trigger conditions

The trigger is based on the total scintillation pulse height observed in individual modules. It differs for wide- and narrow-band beams because of the very large difference in event rates in the two types of beam. The trigger conditions relevant for the selection of charged-current events are as follows:

i) Narrow-band beam trigger: At least three modules give a signal. The required signal level is sufficiently low, so that single muons will trigger with high efficiency. This trigger is effective for all charged-current events, provided a muon of at least 3 GeV is produced.

ii) Wide-band beam trigger: Events are selected if a total of approximately 7 GeV of energy, muonic or hadronic, is deposited anywhere in the apparatus. Since the energy loss of a muon is about 1 GeV per module, the trigger is satisfied even for single muons, provided they pass through more than seven modules.

3.3.2 Reconstruction

The reconstruction of a typical charged-current event by the off-line program is shown in Fig. 4. The hadronic shower energy is computed from the measured scintillator pulse heights on the basis of an algorithm designed to optimize the

energy resolution and to reproduce data obtained with hadronic test beams in the modules [11]. The energy loss of the muon in the shower region is subtracted according to the observed muon momentum.

The muon-momentum reconstruction accounts for the energy loss due to ionization. Radiative losses in excess of $\sim$ 1 GeV are taken into account using the observed pulse height in the scintillators along the track. The muon-track reconstruction has been cross-checked by studying a subset of several thousand events with the help of an interactive program and visual inspection. The efficiency of the muon reconstruction program was found to be 96 ± 1% for events in the fiducial region and with muon momenta larger than 7 GeV. A fraction of the 4% of events which fail in the automatic reconstruction have been reconstructed by hand and compared with the normal events. They show no significant difference in any kinematical quantity.

The energy scale for the muon- and hadron-energy reconstruction has been checked by means of the narrow-band beam events using the fact that the neutrino energy and the radial vertex position are correlated [10]. Events with small $y = E_h/E_\nu$ and large y serve to check the muon- and hadron-energy calibration, respectively.

3.3.3 Selection criteria

Events are accepted provided the following conditions are met:

i) Track length: The muon has to pass through at least five drift chambers. As the hadron shower typically extends over one or two drift chambers only, the remaining event sample has a good muon reconstruction efficiency.

ii) Accuracy of track fit: The probability of the muon fit must be greater than 0.001.

iii) Fiducial volume: The origin of the event must be in the first 13 modules for the narrow-band beam (11 modules for the wide-band beam) within a radius of 1.6 m from the module centre and outside the central excluded region shown in Fig. 2. These fiducial requirements assure complete shower containment and adequate residual track length for the muon track measurement.

iv) Muon momentum: The reconstructed muon momentum must be greater than 7 GeV. This cut is applied only for the narrow-band beam data and is generally more severe than cut (i).

We note that these selection criteria are based on the event origin and the muon; the presence of a hadron shower is not required.

3.3.4 Corrections

The observed event numbers have to be corrected for experimental losses. The narrow-band beam data, which are used for the absolute cross-section measurement, are corrected for the reconstruction inefficiency and the measured dead-time of the detector. For the wide-band beam data a correction (< 6%) is applied to the total event number in each energy bin to account for the trigger inefficiency for events with small hadron energy which originate at the end of the fiducial volume.

The observed event distributions are corrected for acceptance and experimental resolution with the help of a Monte Carlo simulation. In the case of the narrow-band beam, the Monte Carlo events were generated according to the known properties of the neutrino beam and the measured K/π ratios. For the wide-band beam, the energy and radial dependence of the neutrino flux was adjusted to match the observed event distributions. The measurement errors are simulated using the known resolution functions. The observed event numbers in any particular bin of x, y, and Q^2, or ν, are corrected for the effects of acceptance and resolution by multiplying by the ratio of generated-to-accepted Monte Carlo events for the same bin and beam condition. These corrections depend on the x, y, and Q^2 dependence of the cross-sections, which we want to determine. We have approached the true shape of the cross-sections iteratively by repeated comparison of the Monte Carlo simulation with the data.

The average acceptance as a function of y in different x-bins is shown in Fig. 5a for the example of high-energy neutrinos from the decay of 300 GeV/c kaons. The resolution in x for different ranges in Q^2 is shown in Fig. 5b.

4. RESULTS

4.1 Energy dependence of total cross-section

Determination of the absolute cross-sections requires knowledge of the neutrino spectrum and flux. The narrow-band beam fluxes can be calculated from the hadron beam optics, the decay kinematics, and the absolute kaon and pion fluxes. The K/π flux ratios were given in Section 3.2, and the absolute fluxes were determined in two ways: i) on the basis of the absolute hadron flux, as measured with a beam-current transformer; ii) on the basis of the muon fluxes at different depths in the shield, measured by means of solid-state detectors, calibrated by track counting in nuclear emulsions. For the 200 GeV neutrino and antineutrino beams, the two methods are in agreement within 5-10%, and the resulting cross-sections are in agreement with those previously published [3]. However, both methods pose problems, and at 300 GeV the disagreement is greater. We hope to improve our understanding of the absolute neutrino fluxes in the future. For the present, we do not believe that we have made enough progress to publish new absolute cross-sections but content ourselves with normalizing the new results to the published cross-sections [3] in the common energy region. New absolute cross-section results will be postponed to a future experiment.

Although the absolute levels of the cross-sections are normalized to our old result, the energy variation of the cross-sections is new and independent, and for neutrinos extends to higher energies. The results are shown in Fig. 6 and tabulated in Table 2. The error bars include an estimate of the systematic point-to-point error. In addition, table 2 gives also the over-all scale errors owing to the uncertainties of the absolute particle flux measurement and of the K/π ratios. For neutrinos, σ/E_ν shows a drop with energy below $E_\nu \simeq 70$ GeV. No other significant energy dependence is observed, either for neutrinos or antineutrinos, in agreement with other recent results [12] as well as with our previous result [3], but in disagreement with Blair et al. [13]. We note that the measured energy variations are in good agreement with the expectations based on the observed scaling violations as discussed in Section 5.

4.2 Determination of nucleon-structure functions

The first step in the determination of nucleon-structure functions is the tabulation of the differential neutrino and antineutrino cross-sections in bins of x, y, and Q^2, or ν. The correction for acceptance and detector resolution is done with the help of a Monte Carlo simulation as described in Section 3. Bins are accepted only if the unsmearing correction, i.e. the ratio of the true population to the measured population in the bin, differs from one by less than 40%. This selection criterion eliminates essentially all bins with $x > 0.7$, where the majority of observed events has been shifted into this region from smaller values of x owing to resolution effects, and the highest y-bins where the acceptance is low owing to the muon momentum cut.

The differential cross-sections are determined for an isoscalar target, correcting for the small excess of neutrons in the iron nucleus according to the formulae given in the Appendix. Radiative effects are corrected according to the prescription of the De Rujula et al. [14]. These corrections reduce the cross-sections for $x \lesssim 0.2$, increase them for large x, and are generally smaller than 10% except for very small x. Previously, published results [3] as well as preliminary results of the present experiment [15] have used an approximate parametrization for the radiative corrections due to Barlow and Wolfram [16] which differs substantially for small values of x from the present corrections.

The values of the structure functions are evaluated at the centre of the bins in x and Q^2. Fermi-motion effects have not been corrected since they are model-dependent. They mainly affect the shape of the structure functions at large x but have very little effect on the Q^2-dependence. Also no correction has been applied for the suppression of the strange sea due to the threshold effect in the transition $s \to c$.

The expressions which have been used to obtain the structure functions from the differential cross-section measurements are summarized in the Appendix and include all corrections.

4.2.1 Longitudinal structure function

The longitudinal structure function F_L is expected to be non-zero owing to the transverse momentum of the quarks with respect to the nucleon direction which, at high Q^2, can be calculated in perturbative QCD. F_L will also have a contribution if spin-zero constituents such as, for example, diquark systems contribute to neutrino scattering. From an experimental point of view, the longitudinal structure function gives rather small relative contributions to the differential cross-sections in most of the kinematic range so that its determination is subject to severe statistical and systematic errors.

The present analysis uses two different methods to determine the ratio $R = \sigma_L/\sigma_T = F_L/2xF_1$. The first method is based on the sum of neutrino and anti-neutrino differential cross-sections:

$$\frac{d^2\sigma^{\nu}}{dxdy} + \frac{d^2\sigma^{\bar{\nu}}}{dxdy} = \frac{G^2 m_N E_\nu}{\pi} \left\{ \left[1 + (1-y)^2\right] F_2 - y^2 F_L + 2x(s-c)\left[1 - (1-y)^2\right] \right\} . \quad (8)$$

The structure functions F_L and F_2 are separated on the basis of their y-dependence. The second method gives upper limits on R at large x and is based on the expression:

$$\frac{\pi}{G^2 m_N E_\nu} \left[\frac{d^2\sigma^{\bar{\nu}}}{dxdy} - (1-y)^2 \frac{d^2\sigma^{\nu}}{dxdy} \right] \approx \left\{ \bar{q}^{\bar{\nu}} + F_L \left[(1-y) - (1-y)^3\right] - 2x(s-c)(1-y)^2 \right\} , \quad (9)$$

which is approximately valid for $y \gtrsim 0.5$. Experimentally it is observed that the left-hand side is compatible with zero for $x \geq 0.4$ which, in Section 4.2.3, is interpreted as the antiquark distribution being limited to small values of x. According to Eq. (9), this observation can be used to put an upper limit on F_L, keeping in mind that $\bar{q}^{\bar{\nu}}$ has to be larger or equal to zero. This second method is more sensitive and reliable since it is based on the magnitude of the observed cross-sections only.

4.2.1.1 Analysis of the y-dependence

The analysis is based on the 200 GeV narrow-band beam data and has been reported in detail in Ref. [6]. The value of R is determined from the y-distribution for fixed bins in x and ν, i.e. using events from different neutrino energies. The result is free from assumptions about the nature of scaling violations in contrast to previous results which were obtained invoking either Bjorken scaling [17,18] or a definite prescription of scaling violations which was not tested independently [3].

The results for R versus ν, averaged over x and for R versus x averaged over ν are shown in Figs. 7 and 8, respectively. As R does not seem to depend strongly on either ν or x, an average value of R for $\langle\nu\rangle$ = 50 GeV can be obtained by averaging the results in ν or x bins, giving $\langle R\rangle = 0.10 \pm 0.025 \pm 0.06$, where statistical and systematic errors are given in turn. This result depends on the value used for the s-c quark sea. To obtain the above result, we have assumed $x(s-c) = 0.12\ \bar{q}$. A change to $x(s-c) = 0.2\ x(\bar{u} + \bar{d} + \bar{s})$ which is used throughout the rest of this paper, increases R by 0.02. The uncertainty in the amount of strange sea is not included in the systematic error of R.

4.2.1.2 Upper limit on R at large x

Both narrow-band and wide-band beam data are used to evaluate the left-hand side of Eq. (9) in the energy range $20 \leq E_\nu \leq 165$ GeV and for $y \geq 0.44$. The results are summarized in Table 3 for four bins in x. Averaging over the x-range $0.4 \leq x \leq 0.7$, we obtain the result $R \leq 0.039 \pm 0.014 \pm 0.025$ for $\langle Q^2\rangle$ = = 38 GeV^2/c^2, where statistical and systematic errors are given in turn. The main systematic uncertainties are due to the errors in the cross-section ratio $\sigma^{\bar{\nu}}/\sigma^{\nu}$ mainly at small energies and to a smaller extent due to uncertainties in the hadron- and muon-energy calibration. Correction terms proportional to Q^2/ν^2, which have been omitted in Eq. (9) for the sake of simplicity, are important. They have been taken into account in order to derive these results according to the formulae given in the Appendix.

It should be noted that this method gives good upper limits on R only for the x-range where the antiquark contribution is small.

4.2.1.3 Discussion

In Fig. 9 our results, which correspond to an average value of $\langle\nu\rangle \simeq 50$ GeV, are compared with the SLAC-MIT results [20] corresponding to $\langle\nu\rangle$ of about 8 GeV, and the FNAL μp result [21]. The SLAC-MIT experiment measures values of R which are non-zero at large x, outside the given statistical errors, and are in contrast with the QCD expectation. This result has been interpreted as evidence for diquark contributions at large x [22]. The upper limits on R at large x and Q^2 from the present experiment, which are in agreement with the QCD prediction, do not exclude such a diquark contribution since it is expected to disappear very rapidly with Q^2. Comparing the SLAC results with the present analysis, there is an indication of a longitudinal contribution which decreases with Q^2 both at small x and at large x. The measured x-dependence of R is consistent with the QCD prediction. The experimental errors at small x are however still very large.

4.2.2 The structure functions F_2, $2xF_1$, and xF_3

These structure functions are related to the differential cross-sections by the following approximate formulae:

$$F_2 = \frac{\left\{\frac{\pi}{G^2 m_N E_\nu}\left[\frac{d^2\sigma^\nu}{dxdy} + \frac{d^2\sigma^{\bar\nu}}{dxdy}\right] - 2x(s-c)\left[1 - (1-y)^2\right]\right\}}{\left[1 + (1-y)^2 - y^2 R/(1+R)\right]} \tag{10}$$

$$2xF_1 = F_2/(1+R) \tag{11}$$

$$xF_3 = \frac{\pi}{G^2 m_N E_\nu}\left[\frac{d^2\sigma^\nu}{dxdy} - \frac{d^2\sigma^{\bar\nu}}{dxdy}\right] \Big/ \left\{1 - (1-y)^2\right\} \quad . \tag{12}$$

Corrections for non-zero $R = \sigma_L/\sigma_T$ and for the difference s-c have to be applied to obtain the structure function F_2. In Section 4.2 we have seen that the difference between F_2 and $2xF_1$, which is measured by R, is small and that the

uncertainties at the present level of statistics are large compared to it. We therefore extract F_2 under the assumption that R = constant = 0.1. It should be noted that this correction is important only at large y, where the sum of neutrino and antineutrino cross-sections is proportional to $2xF_1$ rather than to F_2. The correction which involves the strange and charmed sea has been evaluated assuming $x[s(x) - c(x)] = 0.2x(\bar{u}+\bar{d}+\bar{s})$, where we have used the result $2xs(x) \approx 0.4x(\bar{u}+\bar{d})$ obtained from the analysis of neutrino- and antineutrino-induced dimuon events [19], and assumed that the charm-quark component xc(x) can be neglected.

The structure functions F_2 and xF_3 have been determined using 200 and 300 GeV narrow-band beam data in the hadron-energy range $E_h < 200$ GeV, where both neutrino and antineutrino data exist.

The results for the three structure functions F_2, $2xF_1$, and xF_3, after all corrections discussed in Section 4.2, are listed in Table 4, including an estimate of the systematic point-to-point errors and the magnitude of the correction to F_2 due to R = 0.1.

The data from the 300 GeV narrow-band beam exposure with hadron energies above 200 GeV, i.e. $y \gtrsim 0.66$, cannot be used to determine F_2 or xF_3 since no useful antineutrino data exist in this energy range. For this reason we use these data to determine the structure function

$$F_+ \equiv \frac{1}{2}\left[2xF_1 + xF_3^{\nu}\right] = x(u+d+2s) \ ,$$

which is obtained using

$$F_+ = \left(\frac{\pi}{G^2 m_N E_\nu}\frac{d^2\sigma^{\nu}}{dxdy} - \left\{x(\bar{u}+\bar{d}+2\bar{c})\left[(1-y)^2 + R(1-y)\right]\right\}\right)\Big/\left[1 + R(1-y)\right] . \qquad (13)$$

The correction term in braces {...}, which is only present in the sea region and is always less than $\sim$ 5% in the kinematic region $y > 0.66$, has been evaluated by an extrapolation of $x(\bar{u}+\bar{d}+2\bar{s})$ from the lower hadron-energy region. The correction

due to R is again evaluated using R = 0.1 and goes to zero for y approaching one. The structure function F_+ is listed in Table 4 for $\nu \gtrsim 100$ GeV using 200 and 300 GeV neutrino data. It should be noted, however, that F_+ is independent of the measurement of F_2 and xF_3 only for $\nu > 200$ GeV.

For x larger than 0.4 the contribution of the sea quarks disappears and the three structure functions $2xF_1 = q + \bar{q}$, $xF_3 = q - \bar{q}$, and $F_+ = q + s$ become progressively the same. The structure functions are displayed in Figs. 10, 11, and 12 as functions of Q^2 and for all bins in x.

4.2.3 The antiquark distribution

The antineutrino cross-section at high y is mainly due to the scattering off antiquarks [Eq. (7)]. Therefore the distribution of sea quarks in the specific combination $\bar{q}^{\bar{\nu}}(x,Q^2) = x(\bar{u}+\bar{d}+2\bar{s})$ is directly measurable. In the narrow-band beam this measurement suffers from statistics owing to low $\bar{\nu}$-flux and the restricted y-range. We have therefore added results from about 155,000 $\bar{\nu}$ and 35,000 ν events with $E_\nu > 20$ GeV which have been recorded in wide-band beams. The evaluation of differential cross-sections is done in the same way as for the narrow-band beam data except that the energy spectrum is obtained from the data themselves, counting all events in a given energy bin. The normalization for the antineutrino is obtained using a linearly rising total cross-section with the slope $\sigma^{\bar{\nu}}/E = 0.30$ (10^{-38} cm^2/GeV). For the neutrino wide-band beam data we use $\sigma/E_\nu = 0.62$ (10^{-38} cm^2/GeV) for $E_\nu > 70$ GeV and a rise of 11% down from 70 GeV to 20 GeV, in agreement with the results of Section 4.2. The differential cross-sections are in good agreement with those from the narrow-band beam. The results of wide-band and narrow-band beams have been averaged. Below $E_\nu \simeq 100$ GeV the wide-band beam data dominate; above, the narrow-band beam data are dominant.

The sea distribution is obtained using $\bar{\nu}$ and ν differential cross-sections for $y > 0.5$ according to the expression:

$$\bar{q}^{\bar{\nu}} = x(\bar{u}+\bar{d}+2\bar{s}) = \left\{ \frac{\pi}{G^2 m_N E_\nu} \left[\frac{d^2\sigma^{\bar{\nu}}}{dxdy} - (1-y)^2 \frac{d^2\sigma^{\nu}}{dxdy} \right] + \right.$$

$$\left. + 2x(s-c)\left[(1-y)^2 - (1-y)^4\right] - F_L\left[(1-y) - (1-y)^3\right] \right\} \Big/ \left[1 - (1-y)^4\right] . \tag{14}$$

The term proportional to $d^2\sigma^{\nu}/dxdy$ subtracts the amount of scattering due to quarks. It is zero at y = 1 and amounts to about 50% at y = 0.5.

The method is illustrated in Fig. 13, which shows $d\sigma^{\bar{\nu}}/dx$ for two energy bins and for four bins in y. The neutrino differential cross-section weighted by $(1-y)^2$ is also shown.

The evaluation of the antiquark distribution requires assumptions about the amount of strange sea and the magnitude of the longitudinal structure function. We use R = 0.1 and $2s/(\bar{u}+\bar{d}) = 0.4$, i.e. the same assumption as for the determination of F_2 and F_+. Experimentally the antiquark structure function is best obtained in bins of x and ν. It is listed in Table 5a together with the estimate of the systematic point-to-point error and the correction due to R = 0.1. The results, translated into bins of x and Q^2, are shown in Fig. 14 together with the result of a QCD fit which will be described in Section 5. Finally, in order to allow an easier comparison with the other structure functions, $\bar{q}^{\bar{\nu}}(x,Q^2)$ is tabulated in the same bins as those used for F_2 and xF_3 in Table 5b.

4.2.4 Discussion of systematic errors

Systematic errors are twofold: i) errors which can be absorbed in an overall scale error, and ii) errors which change the shape and/or the Q^2-slope of the structure functions. The scale error is estimated to be ±6% for F_2 and ±8% for $\bar{q}^{\bar{\nu}}$ and xF_3, mainly due to the error in absolute cross-section measurements. The shapes of the structure functions are affected by the uncertainties in $\sigma^{\bar{\nu}}/\sigma^{\nu}$ and by effects caused by the apparatus, such as errors in the hadron- and muon-energy calibration and in the unfolding of acceptance and resolution effects. The

cross-section ratio $\sigma^{\bar{\nu}}/\sigma^{\nu}$ is well known except for energies below $E_\nu \simeq 50$ GeV [3,12]. This uncertainty gives an error contribution mainly to $\bar{q}^{\bar{\nu}}(x,\nu)$ at low values of ν. The hadron- and muon-energy calibrations have been varied within the estimated uncertainties, and the uncertainty due to resolutions and acceptance effects has been estimated as 15% of the unsmearing correction. All error contributions have been added in quadrature. The results are given in Tables 4 and 5. The systematic errors are always smaller than or at most equal to the statistical errors. They mainly affect the x-dependence of the structure functions but have a smaller effect on their Q^2-dependence.

4.2.5 Dependence of the structure functions on physics assumptions

The structure function $xF_3(x,Q^2)$ is obtained from the differential cross-sections without further assumptions. Unfortunately it is statistically poorly determined owing to the limited statistics of the narrow-band beam data and the fact that it is due to the *difference* of cross-sections. The structure functions F_2, $2xF_1$, F_+, and $\bar{q}^{\bar{\nu}}$, on the other hand, have been extracted under specific assumptions about $R = \sigma_L/\sigma_T$ and the amount of strange and charmed sea. The magnitude of the correction due to R can be seen in Tables 4 and 5a, where the entry ΔR gives the change in the structure function going from R = 0.1 to R = 0. The effect on the measurement of F_2 is generally small compared to the statistical error except in the highest bins of Q^2 for each x bin, since the correction is only substantial at large y. The structure function $2xF_1$, on the other hand, is directly measured at large y only, and therefore suffers from substantial uncertainties in most of our kinematic range. The structure function F_+ is evaluated for high hadron energies ($E_h > 100$ GeV) only, i.e. for $y \gtrsim 0.5$, where the uncertainty due to R is small. This structure function is the most reliable at large x and high values of Q^2. The antiquark distribution finally depends very strongly on R, especially at large values of x. This leaves a substantial uncertainty for $x < 0.4$ where the error in R is still very large.

The effect of the strange-sea correction is very small for $\bar{q}^{\bar{\nu}}$ ($\lesssim 1\%$). The effect on the structure function F_2 is given in Table 6 for two values of $2x(s-c)/\bar{q}(x)$. Here also, the correction is rather small. It should be kept in mind, however, that neutrino interactions with strange quarks lead predominantly to charmed quarks in the final state so that the contribution of $xs(x)$ is kinematically suppressed by a charm mass threshold effect. The magnitude of this suppression can be estimated with the slow rescaling model [23], to be about 0.2 for low hadron energies and 0.8 for the highest energies of this experiment. This leads to scaling violations for the structure functions F_2 and $\bar{q}^{\bar{\nu}}$ at small values of x, which account for up to 30% of the observed slopes in Q^2 at small x-values.

The structure functions have been evaluated assuming an infinite mass for the intermediate vector boson. For a vector boson mass in the range of 80 GeV, the propagator has however a significant effect on the Q^2-slopes at large x.

The structure functions tabulated in Tables 4 and 5 are evaluated under reasonable physics assumptions, given the magnitude of the experimental errors. Any refined analysis has, however, to keep in mind the uncertainties in $R(x,Q^2)$, the effects of the charm mass threshold, and the propagator effect.

5. INTERPRETATION OF STRUCTURE-FUNCTION MEASUREMENTS

5.1 The shape of structure functions

The measurements of $2xF_1$, xF_3, F_+, and $\bar{q}^{\bar{\nu}}$, as described in the previous section, form a consistent set of structure functions for an isoscalar target. Their x-dependences are shown in Fig. 15 for a fixed bin in Q^2, together with empirical fits to the data which fulfil the expected quark parton model relations between these structure functions. The measurements of $2xF_1$ and xF_3 agree at large values of x, and their difference at small x is well described by twice the measured antiquark distribution if the effect of the strange sea is taken into account. An important aspect of the data is that the antiquark contribution disappears for

$x \gtrsim 0.4$, so that $xF_3 \approx 2xF_1$ at large x. Quantitatively, we find $\bar{q}^{\bar{\nu}}/q \lesssim 0.000 \pm$ $\pm$ 0.005 for $x > 0.5$ and an average value of $Q^2 = 33\ GeV^2/c^2$ [7]. Finally, the shape of the strange sea xs(x) has also been measured using $\sim$ 2000 antineutrino-induced opposite-sign dimuon events [19]. Figure 16 shows xs(x) for an average hadronic energy ν = 50 GeV compared to the shape of $\bar{q}^{\bar{\nu}} = x(\bar{u}+\bar{d}+2\bar{s})$, and to $\bar{q}^{\bar{\nu}}$ including the slow rescaling correction. The distributions do not differ by more than the experimental error. The small difference between the two curves shows that the shape of the effective strange-sea structure function is affected very little by the charm threshold discussed in Section 4.2.5.

5.2 Comparison of neutrino and charged-lepton structure functions

In the quark parton model, the structure function $F_2^{\ell N}$ observed in electron or muon inelastic scattering, and the structure function $F_2^{\nu N}$ observed in neutrino scattering, are related outside the sea region by

$$F_2^{\nu N}(x,Q^2) = \frac{18}{5} F_2^{\ell N}(x,Q^2) \ . \qquad (15)$$

In the sea region, neutrino and muon experiments measure different contributions of the strange and charm quarks. For muon experiments the strange sea is suppressed by its quark charge -1/3, whereas in neutrino scattering it is suppressed by the charm threshold effect in the transition $s \to c$. The two effects nearly cancel in the present kinematic range such that the QPM relation (15) should be reasonably well satisfied also at small x. In Fig. 17a our measurements of $F_2^{\nu N}$ are compared with the measurements of $F_2^{\mu N}$ in muon-iron scattering obtained by the European Muon Collaboration (EMC) [24] and with F_2^{ed} obtained in electron-deuteron scattering at SLAC [20]. The EMC data are most easily compared with our data, since the same target material is used and the kinematic range is almost the same. The structure functions $F_2^{\mu N}$ and $F_2^{\nu N}$ agree well in shape within the given statistical and systematic errors, and the normalization agrees with the QPM prediction 18/5. For the SLAC data, on the other hand, we find $F_2^{\nu N}/F_2^{ed} = 1.46 \pm 0.12$ for $x > 0.4$, averaging over the whole Q^2-range including the flux normalization errors on both experiments

where 9/5 = 1.8 is expected. This difference may be related to the uncertainty in R. The agreement with expectation is substantially improved if the value of R is set to zero for the SLAC data at large x and Q^2.

The Q^2-variation d ln F_2/d ln Q^2 of the structure functions $F_2^{\nu N}$ and (18/5) $F_2^{\mu N}$ of Ref. 24 is shown in Fig. 17b as a function of x. The measurements of the slopes have been obtained for each value of x by linear fits in ln Q^2 over the whole available Q^2-range.

Neutrino and muon data show pronounced scaling violations which agree in shape and magnitude. The pattern of scaling violations is well described by leading-order QCD with $\Lambda_{LO} \simeq 0.2$ GeV, as described below.

5.3 Confrontation of structure function measurements with QCD

Perturbative QCD predicts the Q^2-evolution of the nucleon structure functions, although the functions themselves are at present not calculable. The evolution equations as given by Altarelli and Parisi [25] in leading order are

$$\frac{dxF_3(x,Q^2)}{d\ \ln\ Q^2} = \frac{\alpha_s(Q^2)}{2\pi} \int_x^1 \left[Pqq\left(\frac{x}{z}\right) zF_3(z,Q^2)\right] \frac{xdz}{z^2} \qquad (16a)$$

$$\frac{dF_2(x,Q^2)}{d\ \ln\ Q^2} = \frac{\alpha_s(Q^2)}{2\pi} \int_x^1 \left[Pqq\left(\frac{x}{z}\right) F_2(z,Q^2) + 2N_F\ Pgq\left(\frac{x}{z}\right)\ G(z,Q^2)\right] \frac{xdz}{z^2} \qquad (16b)$$

$$\frac{d\bar{q}^{\bar{\nu}}(x,Q^2)}{d\ \ln\ Q^2} = \frac{\alpha_s(Q^2)}{2\pi} \int_x^1 \left[Pqq\left(\frac{x}{z}\right) \bar{q}^{\bar{\nu}}(z,Q^2) + N_F\ Pgq\left(\frac{x}{z}\right)\ G(z,Q^2)\right] \frac{xdz}{z^2} \qquad (16c)$$

$$\frac{dG(x,Q^2)}{d\ \ln\ Q^2} = \frac{\alpha_s(Q^2)}{2\pi} \int_x^1 \left[Pqg\left(\frac{x}{z}\right) F_2(z,Q^2) + Pgg\left(\frac{x}{z}\right)\ G(z,Q^2)\right] \frac{xdz}{z^2} \qquad (16d)$$

In the above equations the P_{ij} are splitting functions given by QCD, $G(x,Q^2)$ is the gluon structure function, N_f is the number of active flavours taken to be four in our range of Q^2, and $\alpha_s = 12\pi/\left[(33-2N_f)\ \ln\ (Q^2/\Lambda^2)\right]$ is the strong coupling constant. The scale parameter Λ is not given by the theory.

The comparison of the inclusive neutrino and antineutrino scattering results with the QCD equations permits conclusions on several distinct points:

i) Tests of the validity of the QCD predictions

ii) The determination of Λ

iii) A determination of the gluon distribution.

All conclusions are based on the measured Q^2-dependence of the structure functions. For tests of the validity of QCD, and for the systematically most correct determination of Λ, the evolution of xF_3, Eq. (16a), is the most useful, since it involves no other structure functions, and is free from uncertainties in $R(x,Q^2)$. The gluon distribution, as well as a statistically superior Λ value, are best determined using both the F_2 and the $\bar{q}^{\bar{\nu}}$ structure functions.

5.3.1 Slopes of structure functions

The predictions of the Altarelli-Parisi equations for the Q^2 evolution of F_2 and $\bar{q}^{\bar{\nu}}$ are compared directly with the measured slopes of the structure functions in Figs. 18a and 18b for $Q_0^2 = 4.5\ GeV^2/c^2$. The data points are obtained by linear fits in $\ln \ln Q^2$ for each value of x. The full curves correspond to the best QCD fit to F_2 and $\bar{q}^{\bar{\nu}}$ as described below. They are in good agreement with the data. On the other hand, non-asymptotically free theories of the strong interaction with scalar or vector gluons are not able to describe the observed scaling violations as shown by the dotted and dashed curves in Fig. 18a and described in detail in another paper [9].

5.3.2 Fitting procedure

The quantitative confrontation of the data with QCD is based on the numerical integration of the Altarelli-Parisi equations (16a) to (16d) using leading- or second-order expressions for $\alpha_s(Q^2)$ and the splitting functions. The structure functions for a starting value $Q^2 = Q_0^2$ have been parametrized in the following way:

$$
\begin{aligned}
xF_3(x,Q_0^2) &= a_3(1 + b_3x)(1 - x)^{c_3} \\
F_2(x,Q_0^2) &= a_2(1 + b_2x)(1 - x)^{c_2} \\
G(x,Q_0^2) &= a_g(1 + b_gx)(1 - x)^{c_g} \\
\bar{q}^{\bar{\nu}}(x,Q_0^2) &= a_q(1 - x)^{c_q} \ .
\end{aligned}
\tag{17}
$$

The parameter a_3 has been fixed by imposing the Gross-Llewellyn Smith sum rule [2] $\int_0^1 F_3 dx = 3$ or $\int_0^1 F_3 dx = 3\left[1-\alpha_s(Q^2)/\pi\right]$ in leading and second order, respectively, and a_g by the momentum sum rule $\int_0^1 G\, dx + \int_0^1 F_2\, dx = 1$. The shape parameters a_i, b_i, c_i, d_i and the scale parameter Λ are then determined by least squares fits to the data†. This method allows the use of all available data in the whole (x,Q^2) range and needs no data at low invariant hadron mass W. In addition, it is rather insensitive to the contributions of unmeasured kinematic regions. We have verified that the above parametrizations are sufficiently general by varying Q_0^2. We note, however, that the effects due to b_i being non-zero are quite significant for the quality of the fits and the results.

Quantumchromodynamic fits have been performed to the non-singlet structure function xF_3, and to the singlet structure functions F_2 and $\bar{q}^{\bar{\nu}}$. These fits use only data with $Q^2 > 2$ GeV$^2/c^2$ and $W^2 > 11$ GeV^2. The low Q^2 cut is justified *a posteriori* by the small value of Λ obtained in these fits. The W cut was imposed to avoid the kinematic region where higher twist contributions may be expected to be important and where non-leading corrections are substantial. Target mass corrections are applied according to the prescription of Ref. [26]. Finally, we include a propagator term with a mass $m_W = 80$ GeV.

5.3.3 Analysis of the non-singlet structure function xF_3

The Q^2 evolution of xF_3 as given by Eq. (15a) is most easily obtained as it does not involve the gluon distribution. The result of the second-order fit is compared with the measurements in Fig. 11. The best value for Λ is $\Lambda_{\overline{MS}} = 0.2\ ^{+\ 0.2}_{-\ 0.1}$ GeV including our estimate of the systematic uncertainties. This

† We have used the programs developed by Abbott and Barnett, for the numerical solution of the Altarelli-Parisi equation. The second-order calculations for the non-singlet case have been verified using the program of Lopez and Yndurain.

result is not only independent of assumptions about the shape of the gluon distribution, it is also not affected by the uncertainties on the value of R, the amount of the strange sea and the threshold effects due to charm production. This result is therefore most significant from a systematic point of view.

5.3.4 Combined analysis of F_2 and $\bar{q}^{\bar{\nu}}$

The QCD predictions for the Q^2-evolution of F_2 and $\bar{q}^{\bar{\nu}}$ involve the unknown gluon structure function $G(x,Q_0^2)$ and the scale parameter Λ. The analysis of F_2 alone is unable to determine Λ and $G(x,Q_0^2)$ simultaneously since Λ is very strongly correlated to the width of the gluon distribution. If the functional form of the gluon distribution is not constrained, no separation between the effects of Λ and the gluon distribution is possible with F_2 alone. The additional measurement of $\bar{q}^{\bar{\nu}}$, however, provides the means for the separation of the two. This can be seen in two ways:

i) Λ can be determined from the Q^2-evolution of F_2 at large x, i.e. $x \gtrsim 0.3$ after subtracting the sea-quark contribution to get the "non-singlet" structure function

$$\begin{aligned} F_{NS}(x,Q^2) &\equiv F_2(x,Q^2) - 2\left[\bar{q}^{\bar{\nu}} - xs(x,Q^2)\right] \\ &\approx F_2(x,Q^2) - 1.7\ \bar{q}^{\bar{\nu}} \ . \end{aligned} \tag{18}$$

For $x > 0.3$ the correction is small and well known. Note also that R is well determined in this x-range and is practically zero such that we are justified in analysing F_{NS} as a non-singlet structure function.

ii) The gluon distribution can be determined by a simultaneous analysis of F_2 and $\bar{q}^{\bar{\nu}}$ including the sea region, leaving both $G(x,Q_0^2)$ and Λ as unknowns. In this analysis we use mainly the fact that $\bar{q}^{\bar{\nu}}$ is very small at large x. A broad gluon distribution leads to a rise of the antiquark distribution at large x with Q^2 due to the convolution $Pgq \otimes G(x,Q^2)$ in Eq. (16c) such that the QCD prediction will be above the measured $\bar{q}^{\bar{\nu}}$ even if we start with a vanishing $\bar{q}$-distribution at small Q^2 (say $Q^2 = 2\ GeV^2/c^2$). From the point of systematic

uncertainties, the magnitude of $\bar{q}^{\bar{\nu}}$ at large x is well measured and more reliable than the measurement of scaling violations. It should be noted that the values of $\bar{q}^{\bar{\nu}}$ from Table 5 which are given for R = 0.1 for all x, should be corrected to R = 0, at large x, in agreement with the results of Section 4.2.1.2.

5.3.4.1 Non-singlet analysis of F_2 at large x

The structure function F_2 is most accurately determined from a statistical point of view. If the analysis is restricted to large x where R is well bounded and the sea contribution small, the uncertainties due to $R = \sigma_L/\sigma_T$ and the charm threshold are negligible. We choose $x > 0.3$ and subtract the small sea-quark contribution according to Eq. (18) using our measurement of $\bar{q}^{\bar{\nu}}$. The structure functions F_2 and $\bar{q}^{\bar{\nu}}$ are evaluated using the QCD prediction for R in agreement with the upper limits derived in Section 4.2.1.2.

The results of leading and second-order fits are summarized in Table 7. We find $\Lambda_{\overline{MS}} = 0.30 \pm 0.075$ GeV in agreement with the results of the non-singlet fits to xF_3 and the combined singlet fit to F_2 and $\bar{q}^{\bar{\nu}}$.

The dependence of Λ on various systematic effects and different cuts is summarized in Table 8. Whereas target mass corrections and Fermi-motion correction lead to small variations only, the weak propagator has a substantial influence on the result. Previous results which have been reported for the same data [27] had been obtained using a value of R = 0.1 which reduces the value of Λ by 0.1 GeV.

Including our estimate of the systematic uncertainties, the non-singlet analysis of F_2 at large x gives the result $\Lambda_{\overline{MS}} = 0.30 \pm 0.15$ GeV.

5.3.4.2 Determination of the gluon distribution by an analysis of F_2 and $\bar{q}^{\bar{\nu}}$

The combined analysis of F_2 and $\bar{q}^{\bar{\nu}}$ allows a simultaneous determination of Λ and the gluon distribution as discussed in detail in Ref. [8]. The result of the leading-order QCD fit to the tabulated structure functions is given in Table 7. It is compared with the measured structure functions in Figs. 10 and 14 and with the measured slopes in Fig. 18. The structure functions G(x), $F_2(x)$, and $\bar{q}^{\bar{\nu}}(x)$ as given by this fit are shown in Fig. 19 for a fixed value of Q^2.

The gluon distribution can only be determined if the observed scaling violations are due to QCD effects. Unfortunately the Q^2-dependence of F_2 and $\bar{q}^{\bar{\nu}}$ is subject to substantial uncertainties due to the charm threshold effect for the strange sea contribution and the poor knowledge of R at small values of x. The magnitude of these effects is estimated in Fig. 20 for the slopes of F_2 using the QCD prediction for $R(x,Q^2)$ and the slow rescaling model for the charm threshold effect. The small x region ($x \lesssim 0.3$) is seriously affected, whereas the large x region shows only a weak dependence. The slopes of $\bar{q}^{\bar{\nu}}$ at small x are affected even more severely by these uncertainties. These effects have been studied in Ref. [8] using different assumptions about the strange- and charmed-sea distribution and about R with the result that the gluon distribution was only moderately affected by these effects. Meanwhile we have obtained upper limits on R at large x, such that the uncertainties of the $\bar{q}^{\bar{\nu}}$ measurement and the slopes of F_2 at large x are reduced and we can hope to get a more reliable estimate of $G(x,Q_0^2)$.

We have therefore repeated the singlet analysis using R equal to the QCD prediction which at large x agrees well with the upper limits of Section 4.2.1.2. In order to eliminate the regions with large uncertainties due to R at small x, we use F_2 for $0.03 < x < 0.7$ and $\bar{q}^{\bar{\nu}}$ for $0.3 < x < 0.7$ only. Finally we correct F_2 for the charm threshold effect using the slow rescaling model [23] with an effective mass of the charm quark $m_c = 1.5\ \mathrm{GeV}/c^2$. The result of this fit is also given in Table 7. The gluon distribution comes out slightly broader compared to the fits with R = 0.1 and Λ_{LO} increases to 0.29 GeV.

Clearly, the shape of the gluon distribution depends on the functional form which is chosen for the reference value Q_0^2. Our parametrization (17) involves only two free parameters. It gives nevertheless substantial freedom for the shape of the distribution. Within the given parametrization, the gluon distribution is well determined because the integral of $G(x,Q_0^2)$ is given by the energy-momentum sum rule and the width is constrained by the measured width of the antiquark distribution.

The effect of second-order QCD corrections has been studied by several authors [28]. The effect on the gluon distribution is small and comparable to the experimental uncertainties.

We conclude that the combined analysis of F_2 and $\bar{q}^{\bar{\nu}}$ has provided, for the first time, a determination of the gluon distribution.

5.3.5 Conclusions

The Q^2-dependence of all structure functions at high values of the invariant hadron mass ($W^2 > 11$ GeV^2) is consistently described by QCD with a value of Λ around 0.25 GeV. It is incompatible with the predictions of non-asymptotically-free theories of the strong interactions as discussed in detail in Ref. [9].

The magnitude of non-perturbative contributions, on the other hand, cannot be estimated reliably. If there is just one higher twist term, then the scaling violations at high W are dominated by QCD effects and our determination of Λ and the gluon distribution remain unaffected. In principle, however, all scaling violations could be explained by more complicated higher twist contributions, provided they mimic the x-dependence of QCD [29]. Except for this improbable possibility, we have achieved a reliable determination of Λ and the gluon distribution. The results summarized in Tables 7 and 8 can be combined to obtain a best value of Λ from the present experiment. Including our estimate of systematic uncertainties we find $\Lambda_{\overline{MS}} = 0.25 \,^{+\,0.15}_{-\,0.1}$ GeV.

6. GENERAL CONCLUSIONS

We list here the more important results of this experiment:

i) The neutrino and antineutrino cross-sections are proportional to E_ν at energies above $\sim$ 70 GeV. For the neutrino cross-section, σ^ν/E shows a significant rise towards lower energies in agreement with the pattern of the observed scaling violations.

ii) The complete and consistent set of structure functions F_2, xF_3, $\bar{q}^{\bar{\nu}}$ and $xs(x)$ has been determined for an isoscalar target in the Q^2-range $1 < Q^2 < 200\ GeV^2/c^2$. It is more precise and comprehensive than measurements previously available and provides a reliable basis for the study of parton dynamics in hard scattering processes. The measurement of F_2 agrees well with similar measurements in charged-lepton scattering, in agreement with the quark parton model.

iii) A deviation from the Callan-Gross relation is observed at small x, whereas the longitudinal structure function is negligible at large x in agreement with the QCD expectation.

iv) Clear scaling violations are observed for all structure functions. The observed Q^2-dependence for $W^2 > 11\ GeV^2$ is in good agreement with QCD but at variance with non-asymptotically free theories of the strong interaction.

v) The combined analysis of F_2 and $\bar{q}^{\bar{\nu}}$ has, for the first time, allowed a determination of the gluon structure function.

vi) The value of Λ obtained from data at $W^2 > 11\ GeV^2$ is $\Lambda_{\overline{MS}} = 0.25\ ^{+\ 0.15}_{-\ 0.10}$, including an estimate of systematic errors.

Acknowledgements

We thank our technical staff, from all the participating institutions, who have contributed so much to the construction and running of the detector. We also thank H. Wind for important contributions to the muon reconstruction program. We thank M. Barnett and C. Lopez for helpful discussions concerning the QCD comparisons.

REFERENCES

[1] C.G. Callan and D.J. Gross, Phys. Rev. Lett. 22, 156 (1969).

[2] D.J. Gross and C.H. Llewellyn Smith, Nucl. Phys. B14, 337 (1969).

[3] J.G.H. de Groot et al., Z. Phys. C1, 143 (1979).

[4] J.G.H. de Groot et al., Phys. Lett. 82B, 292 (1979).

[5] J.G.H. de Groot et al., Phys. Lett. 82B, 456 (1979).

[6] H. Abramowicz et al., Phys. Lett. 107B, 141 (1981).

[7] H. Abramowicz et al., Z. Phys. C12, 225 (1982).

[8] H. Abramowicz et al., Z. Phys. C12, 289 (1982).

[9] H. Abramowicz et al., Z. Phys. C13, 199 (1982).

[10] M. Holder et al., Nucl. Instrum. Methods 148, 235 (1978).

[11] H. Abramowicz et al., Nucl. Instrum. Methods 180, 429 (1981).

[12] For a recent compilation of total cross-section measurements, see, for example, H. Wahl, Proc. 16th Rencontre de Moriond, Les Arcs, 1981 (Editions Frontières, Dreux, 1981), p. 233.

[13] R. Blair et al. (CCFRR Collaboration), Proc. Neutrino '81 Conf., Hawaii, 1981 (High-Energy Physics Group, Univ. of Hawaii, Honolulu, 1981), p. 311.

[14] A. De Rújula et al., Nucl. Phys. B154, 394 (1979).

[15] F. Eisele, Proc. Int. Conf. on Neutrino Physics and Astrophysics, Erice, 1980 (ed. L. Fiorini) (Plenum Press, NY, 1982) p. 143.

[16] R. Barlow and S. Wolfram, Phys. Rev. D20, 2198 (1979).

[17] M. Jonker et al., Phys. Lett. 109B, 133 (1982).

[18] S.M. Heagy et al., Phys. Rev. D23, 1045 (1981).

[19] H. Abramowicz et al., Z. Phys. C15, 19 (1982).

[20] A. Bodek et al., Phys. Rev. D20, 1471 (1979).

[21] B.A. Gordon et al., Phys. Rev. D20, 2645 (1979).

[22] L.F. Abbott et al., Phys. Rev. D22, 582 (1980).

[23] R.M. Barnett, Phys. Rev. D14, 70 (1976).

[24] J.J. Aubert et al., Phys. Lett. 105B, 322 (1981).

[25] G. Altarelli and G. Parisi, Nucl. Phys. B126, 298 (1979).

[26] R. Barbieri et al., Nucl. Phys. B117, 50 (1976).
H. Georgi and H.D. Politzer, Phys. Rev. D14, 1829 (1976).

[27] F. Eisele et al. (CDHS Collaboration), Proc. Neutrino '81 Conf., Hawaii, 1981 (High-Energy Physics Group, Univ. of Hawaii, Honolulu, 1981), p. 297.

[28] L. Baulieu and C. Kounnas, preprint TH.3266-CERN (1982).
D. Duke, private communication.

[29] F. Eisele et al., Phys. Rev. D26, 41 (1982).

[30] B. Pszola (CDHS Collaboration), Proc. Neutrino '82 Conf., Balat›nfüred, 1982 (eds. A. Frenkel and L. Jenik, 1982), Vol. II, p. 133.

Table 1

Characteristics of the five exposures used in this paper

Type of beam	Main characteristics	Number of protons on target	Number of charged-current events, after cuts
200 GeV νNBB	Positive, momentum-selected hadrons, $\Delta p/p = \pm 5\%$, $\Omega \simeq 15$ μsr	1.1×10^{18}	62,000
200 GeV $\bar{\nu}$NBB	Negative, momentum-selected hadrons, $\Delta p/p \simeq \pm 5\%$, $\Omega \simeq 15$ μsr	2.9×10^{18}	26,000
300 GeV νNBB	Positive, momentum-selected hadrons, $\Delta p/p \simeq \pm 5\%$, $\Omega \simeq 10$ μsr	2.4×10^{18}	32,000
350 GeV $\bar{\nu}$WBB	Horn-focused beam, negative particles focused, 350 GeV protons on target	4.3×10^{17}	155,000
350 GeV νWBB	Horn-focused beam, positive particles focused, 350 GeV protons on target	0.3×10^{17}	35,000

Table 2

Energy dependence of total neutrino and antineutrino cross-section from 200 and 300 GeV narrow-band beams. The systematic errors given are the estimated point-to-point errors due to energy calibration and resolution. The absolute normalization is fixed to yield $\sigma^{\nu}/E = 0.62$ and $\sigma^{\bar{\nu}}/E = 0.30$ in the energy range $30 < E_{\nu} < 90$ GeV, in agreement with the published results [3]. Both cross-section slopes have an additional over-all scale errors.

Neutrino energy bin	σ^{ν}/E_{ν} ($\times 10^{38}$ cm^{-2} GeV)		$\sigma^{\bar{\nu}}/E_{\bar{\nu}}$ ($\times 10^{38}$ cm^{-2} GeV)	
(GeV)	Value $\pm \sigma_{stat} \pm \sigma_{syst}$	Scale error	Value $\pm \sigma_{stat} \pm \sigma_{syst}$	Scale error
30-40	0.660 ± 0.015 ± 0.009		0.319 ± 0.009 ± 0.006	
40-50	0.649 ± 0.013 ± 0.012		0.297 ± 0.008 ± 0.005	
50-60	0.618 ± 0.011 ± 0.011	±6%	0.303 ± 0.007 ± 0.006	±5%
60-70	0.615 ± 0.010 ± 0.010		0.285 ± 0.006 ± 0.005	
70-80	0.599 ± 0.008 ± 0.004		0.297 ± 0.006 ± 0.002	
80-90	0.584 ± 0.009 ± 0.010		0.279 ± 0.007 ± 0.010	
90-100	0.611 ± 0.013 ± 0.007		0.287 ± 0.019 ± 0.008	
100-115	0.594 ± 0.009 ± 0.005		0.294 ± 0.013 ± 0.007	
115-130	0.588 ± 0.009 ± 0.010		0.271 ± 0.011 ± 0.009	
130-145	0.605 ± 0.009 ± 0.006		0.274 ± 0.010 ± 0.006	
145-160	0.597 ± 0.008 ± 0.006		0.287 ± 0.010 ± 0.005	
160-175	0.610 ± 0.008 ± 0.004	±7.2%	0.302 ± 0.010 ± 0.006	±6.5%
175-190	0.600 ± 0.009 ± 0.005		0.303 ± 0.018 ± 0.010	
190-205	0.595 ± 0.014 ± 0.009			
205-225	0.582 ± 0.012 ± 0.006			
225-245	0.572 ± 0.011 ± 0.008			
245-265	0.582 ± 0.012 ± 0.012			
265-285	0.595 ± 0.013 ± 0.015			

Table 3

Upper limits for $R = \sigma_L/\sigma_T$ at large x

x	0.35	0.45	0.55	0.65
$R = \sigma_L/\sigma_T \leq$	0.152	0.058	0.022	0.017
σ_{stat}	0.019	0.019	0.024	0.033
σ_{syst}	0.042	0.022	0.025	0.035
$\langle Q^2 \rangle$ $[GeV^2/c^2]$	30.0	37.0	39.0	37.0

Table 4

Structure functions F_2, $2xF_1$, xF_3, and F_+.
The structure functions are evaluated at the bin centre with the assumptions $R = \sigma_L/\sigma_T = 0.1$ and $m_W = \infty$. No correction for Fermi motion has been applied. The errors given are statistical and systematic point-to-point errors. In addition we have an over-all scale error of ±6% for F_2 and F_+ and ±8% for xF_3. The column ΔR gives the change in F_2 if R is changed from zero to 0.1.

Q^2 (GeV^2/c^2)	x	$F_2 \pm \sigma_{stat} \pm \sigma_{syst}$	ΔR	$2xF_1 \pm \sigma_{stat}$	x	$xF_3 \pm \sigma_{stat} \pm \sigma_{syst}$	$F_+ \pm \sigma_{stat} \pm \sigma_{syst}$
1.13	0.015	0.697 ± 0.077 ± 0.08	0.007	0.634 ± 0.070	0.015	0.160 ± 0.090 ± 0.08	
	0.045	0.754 ± 0.073 ± 0.08	0.001	0.689 ± 0.067			
	0.080	0.916 ± 0.081 ± 0.08	0.000	0.850 ± 0.075			
	0.150	0.940 ± 0.071 ± 0.05	0.000	0.915 ± 0.069			
1.42	0.015	0.838 ± 0.055 ± 0.05	0.007	0.762 ± 0.050	0.015	0.178 ± 0.077 ± 0.08	
	0.045	0.913 ± 0.062 ± 0.05	0.001	0.834 ± 0.057	0.045	0.345 ± 0.150 ± 0.05	
	0.080	0.983 ± 0.079 ± 0.05	0.000	0.908 ± 0.073			
	0.150	0.882 ± 0.057 ± 0.03	0.000	0.846 ± 0.055			
1.79	0.015	0.901 ± 0.060 ± 0.05	0.012	0.819 ± 0.054	0.015	0.249 ± 0.074 ± 0.07	
	0.045	0.950 ± 0.062 ± 0.05	0.003	0.867 ± 0.056	0.045	0.310 ± 0.128 ± 0.07	
	0.080	1.038 ± 0.070 ± 0.05	0.001	0.956 ± 0.065	0.080	0.853 ± 0.264 ± 0.07	
	0.150	0.934 ± 0.054 ± 0.05	0.000	0.887 ± 0.051			
	0.250	0.833 ± 0.071 ± 0.05	0.000	0.851 ± 0.072			
2.25	0.015	0.807 ± 0.056 ± 0.05	0.016	0.734 ± 0.051	0.015	0.311 ± 0.067 ± 0.07	
	0.045	1.025 ± 0.062 ± 0.05	0.005	0.935 ± 0.057	0.045	0.261 ± 0.105 ± 0.07	
	0.080	1.095 ± 0.067 ± 0.05	0.001	1.005 ± 0.061	0.080	0.524 ± 0.183 ± 0.07	
	0.150	0.910 ± 0.047 ± 0.05	0.000	0.856 ± 0.044	0.150	0.818 ± 0.244 ± 0.07	
	0.250	0.772 ± 0.058 ± 0.05	0.000	0.771 ± 0.058			
	0.350	0.577 ± 0.059 ± 0.05	0.000	0.625 ± 0.063			
2.84	0.015	1.065 ± 0.086 ± 0.04	0.018	0.969 ± 0.078	0.015	0.284 ± 0.109 ± 0.06	0.710 ± 0.055 ± 0.04
	0.045	0.838 ± 0.051 ± 0.04	0.004	0.764 ± 0.046	0.045	0.103 ± 0.072 ± 0.06	
	0.080	1.031 ± 0.059 ± 0.04	0.001	0.945 ± 0.054	0.080	0.473 ± 0.143 ± 0.06	
	0.150	0.946 ± 0.046 ± 0.04	0.000	0.884 ± 0.043	0.150	0.455 ± 0.195 ± 0.06	
	0.250	0.803 ± 0.054 ± 0.04	0.000	0.787 ± 0.053			
	0.350	0.612 ± 0.054 ± 0.04	0.000	0.641 ± 0.056			
	0.450	0.520 ± 0.053 ± 0.04	0.000	0.592 ± 0.060			
3.57	0.015	1.178 ± 0.099 ± 0.04	0.031	1.071 ± 0.090	0.015	0.278 ± 0.112 ± 0.06	0.746 ± 0.056 ± 0.04
	0.045	1.087 ± 0.058 ± 0.04	0.007	0.990 ± 0.053	0.045	0.390 ± 0.082 ± 0.06	
	0.080	1.105 ± 0.056 ± 0.03	0.003	1.011 ± 0.050	0.080	0.553 ± 0.117 ± 0.06	
	0.150	1.018 ± 0.043 ± 0.03	0.001	0.946 ± 0.040	0.150	0.468 ± 0.140 ± 0.06	
	0.250	0.762 ± 0.045 ± 0.03	0.000	0.735 ± 0.044	0.250	0.394 ± 0.289 ± 0.06	
	0.350	0.697 ± 0.053 ± 0.03	0.000	0.710 ± 0.053			
	0.450	0.507 ± 0.045 ± 0.03	0.000	0.553 ± 0.049			
	0.550	0.345 ± 0.039 ± 0.04	0.000	0.408 ± 0.046			
4.50	0.015	1.059 ± 0.097 ± 0.06	0.037	0.963 ± 0.088	0.015	0.211 ± 0.103 ± 0.06	0.631 ± 0.051 ± 0.06
	0.045	1.097 ± 0.057 ± 0.04	0.019	0.999 ± 0.052	0.045	0.282 ± 0.071 ± 0.06	
	0.080	1.000 ± 0.049 ± 0.03	0.006	0.914 ± 0.044	0.080	0.448 ± 0.080 ± 0.05	
	0.150	1.003 ± 0.038 ± 0.03	0.001	0.928 ± 0.035	0.150	0.716 ± 0.110 ± 0.05	
	0.250	0.854 ± 0.046 ± 0.03	0.000	0.814 ± 0.044	0.250	0.901 ± 0.230 ± 0.05	
	0.350	0.619 ± 0.043 ± 0.03	0.000	0.617 ± 0.043			
	0.450	0.446 ± 0.039 ± 0.03	0.000	0.470 ± 0.042			
	0.550	0.310 ± 0.033 ± 0.03	0.000	0.349 ± 0.037			

Q^2 (GeV^2/c^2)	x	$F_2 \pm \sigma_{stat} \pm \sigma_{syst}$	ΔR	$2xF_1 \pm \sigma_{stat}$	x	$xF_3 \pm \sigma_{stat} \pm \sigma_{syst}$	$F_+ \pm \sigma_{stat} \pm \sigma_{syst}$
5.66	0.015	1.078 ± 0.110 ± 0.08	0.057	0.980 ± 0.100	0.015	0.538 ± 0.108 ± 0.06	0.750 ± 0.065 ± 0.06
	0.045	1.147 ± 0.067 ± 0.04	0.034	1.044 ± 0.061	0.045	0.373 ± 0.074 0.06	
	0.080	1.142 ± 0.052 ± 0.03	0.010	1.043 ± 0.047	0.080	0.475 ± 0.073 0.06	
	0.150	1.073 ± 0.037 ± 0.03	0.003	0.989 ± 0.034	0.150	0.707 ± 0.082 0.06	
	0.250	0.789 ± 0.039 ± 0.03	0.000	0.745 ± 0.036	0.250	0.575 ± 0.141 0.04	
	0.350	0.658 ± 0.041 ± 0.03	0.000	0.644 ± 0.040	0.350	0.745 ± 0.224 0.04	
	0.450	0.440 ± 0.035 ± 0.02	0.000	0.451 ± 0.036	0.450	0.527 ± 0.274 0.04	
	0.550	0.237 ± 0.026 ± 0.02	0.000	0.256 ± 0.028			
	0.650	0.170 ± 0.033 ± 0.03	0.000	0.196 ± 0.037			
7.13	0.015				0.015		0.637 ± 0.076 ± 0.08
	0.045	1.149 ± 0.065 ± 0.04	0.031	1.046 ± 0.059	0.045	0.490 ± 0.074 0.06	0.814 ± 0.046 ± 0.03
	0.080	1.171 ± 0.052 ± 0.03	0.012	1.067 ± 0.048	0.080	0.601 ± 0.072 0.05	
	0.150	1.025 ± 0.034 ± 0.03	0.004	0.942 ± 0.031	0.150	0.593 ± 0.061 0.04	
	0.250	0.791 ± 0.036 ± 0.03	0.001	0.742 ± 0.033	0.250	0.618 ± 0.100 0.04	
	0.350	0.600 ± 0.036 ± 0.02	0.000	0.579 ± 0.035	0.350	0.450 ± 0.150 0.04	
	0.450	0.474 ± 0.036 ± 0.02	0.000	0.474 ± 0.035	0.450	0.664 ± 0.195 0.04	
	0.550	0.287 ± 0.026 ± 0.02	0.000	0.301 ± 0.027	0.550	0.185 ± 0.230 0.04	
	0.650	0.122 ± 0.023 ± 0.03	0.000	0.134 ± 0.025			
8.97	0.045	1.225 ± 0.075 ± 0.04	0.042	1.114 ± 0.068	0.045	0.610 ± 0.080 0.06	0.913 ± 0.051 ± 0.04
	0.080	1.086 ± 0.049 ± 0.03	0.014	0.990 ± 0.045	0.080	0.531 ± 0.060 0.04	
	0.150	0.987 ± 0.031 ± 0.03	0.006	0.905 ± 0.028	0.150	0.620 ± 0.047 0.04	
	0.250	0.838 ± 0.033 ± 0.03	0.001	0.780 ± 0.039	0.250	0.668 ± 0.077 0.04	
	0.350	0.573 ± 0.032 ± 0.02	0.000	0.546 ± 0.030	0.350	0.383 ± 0.100 0.04	
	0.450	0.424 ± 0.030 ± 0.02	0.000	0.416 ± 0.029	0.450	0.446 ± 0.139 0.03	
	0.550	0.247 ± 0.023 ± 0.02	0.000	0.251 ± 0.023	0.550	0.361 ± 0.114 0.03	
	0.650	0.171 ± 0.026 ± 0.02	0.000	0.182 ± 0.027	0.650	0.097 ± 0.158 0.03	
11.3	0.045	1.286 ± 0.088 ± 0.05	0.060	1.161 ± 0.080	0.045	0.580 ± 0.087 ± 0.08	0.897 ± 0.052 ± 0.05
	0.080	1.224 ± 0.058 ± 0.04	0.028	1.115 ± 0.053	0.080	0.572 ± 0.068 ± 0.06	
	0.150	1.080 ± 0.033 ± 0.03	0.009	0.987 ± 0.030	0.150	0.686 ± 0.047 ± 0.04	
	0.250	0.850 ± 0.031 ± 0.02	0.003	0.785 ± 0.029	0.250	0.681 ± 0.060 ± 0.03	
	0.350	0.591 ± 0.030 ± 0.02	0.001	0.558 ± 0.028	0.350	0.545 ± 0.083 ± 0.02	
	0.450	0.380 ± 0.025 ± 0.02	0.000	0.367 ± 0.024	0.450	0.369 ± 0.084 ± 0.02	
	0.550	0.230 ± 0.020 ± 0.02	0.000	0.227 ± 0.020	0.550	0.237 ± 0.114 ± 0.02	
	0.650	0.155 ± 0.042 ± 0.02	0.000	0.160 ± 0.043			
14.2	0.045	1.215 ± 0.130 ± 0.08	0.079	1.105 ± 0.119	0.045	0.390 ± 0.122 ± 0.10	0.835 ± 0.056 ± 0.05
	0.080	1.108 ± 0.060 ± 0.03	0.032	1.009 ± 0.054	0.080	0.560 ± 0.066 ± 0.04	0.849 ± 0.040 ± 0.03
	0.150	1.046 ± 0.030 ± 0.02	0.013	0.956 ± 0.028	0.150	0.725 ± 0.039 ± 0.03	
	0.250	0.772 ± 0.028 ± 0.02	0.004	0.713 ± 0.025	0.250	0.543 ± 0.046 ± 0.02	
	0.350	0.556 ± 0.025 ± 0.02	0.001	0.521 ± 0.024	0.350	0.500 ± 0.056 ± 0.02	
	0.450	0.356 ± 0.022 ± 0.015	0.001	0.340 ± 0.021	0.450	0.398 ± 0.067 ± 0.015	
	0.550	0.233 ± 0.015 ± 0.015	0.000	0.228 ± 0.018	0.550	0.357 ± 0.071 ± 0.015	
	0.650	0.133 ± 0.015 ± 0.01	0.000	0.133 ± 0.015	0.650	0.145 ± 0.079 ± 0.01	
17.9	0.045				0.045		0.809 ± 0.077 ± 0.06
	0.080	1.275 ± 0.068 ± 0.04	0.053	1.161 ± 0.062	0.080	0.584 ± 0.069 ± 0.05	0.920 ± 0.043 ± 0.04
	0.150	1.012 ± 0.030 ± 0.02	0.015	0.924 ± 0.028	0.150	0.648 ± 0.038 ± 0.03	
	0.250	0.797 ± 0.027 ± 0.02	0.006	0.733 ± 0.025	0.250	0.630 ± 0.040 ± 0.02	
	0.350	0.602 ± 0.025 ± 0.02	0.003	0.561 ± 0.024	0.350	0.476 ± 0.045 ± 0.02	
	0.450	0.366 ± 0.021 ± 0.015	0.001	0.346 ± 0.020	0.450	0.313 ± 0.048 ± 0.015	
	0.550	0.241 ± 0.018 ± 0.015	0.000	0.232 ± 0.017	0.550	0.262 ± 0.050 ± 0.015	
	0.650	0.106 ± 0.013 ± 0.01	0.000	0.105 ± 0.013	0.650	0.083 ± 0.062 ± 0.01	

Q^2 (GeV^2/c^2)	x	$F_2 \pm \sigma_{stat} \pm \sigma_{syst}$	ΔR	$2xF_1 \pm \sigma_{stat}$	x	$xF_3 \pm \sigma_{stat} \pm \sigma_{syst}$	$F_+ \pm \sigma_{stat} \pm \sigma_{syst}$
22.5	0.045				0.045		0.864 ± 0.117 ± 0.08
	0.080	1.207 ± 0.078 ± 0.06	0.060	1.098 ± 0.070	0.080	0.729 ± 0.075 ± 0.08	0.931 ± 0.050 ± 0.06
	0.150	0.998 ± 0.031 ± 0.02	0.023	0.910 ± 0.029	0.150	0.710 ± 0.036 ± 0.03	0.827 ± 0.026 ± 0.02
	0.250	0.764 ± 0.026 ± 0.02	0.010	0.701 ± 0.023	0.250	0.592 ± 0.034 ± 0.02	
	0.350	0.559 ± 0.023 ± 0.02	0.002	0.518 ± 0.022	0.350	0.509 ± 0.039 ± 0.02	
	0.450	0.396 ± 0.021 ± 0.015	0.001	0.371 ± 0.020	0.450	0.336 ± 0.038 ± 0.015	
	0.550	0.231 ± 0.016 ± 0.015	0.000	0.220 ± 0.015	0.550	0.296 ± 0.038 ± 0.015	
	0.650	0.110 ± 0.011 ± 0.01	0.000	0.106 ± 0.011	0.650	0.142 ± 0.038 ± 0.01	
28.4	0.080	1.128 ± 0.121 ± 0.08	0.078	1.026 ± 0.110	0.080	0.625 ± 0.110 ± 0.08	0.859 ± 0.056 ± 0.06
	0.150	1.071 ± 0.036 ± 0.03	0.035	0.976 ± 0.033	0.150	0.727 ± 0.039 ± 0.04	0.860 ± 0.026 ± 0.03
	0.250	0.802 ± 0.027 ± 0.02	0.013	0.735 ± 0.025	0.250	0.604 ± 0.034 ± 0.03	
	0.350	0.544 ± 0.022 ± 0.015	0.006	0.502 ± 0.020	0.350	0.456 ± 0.030 ± 0.015	
	0.450	0.335 ± 0.017 ± 0.015	0.002	0.312 ± 0.016	0.450	0.314 ± 0.028 ± 0.015	
	0.550	0.204 ± 0.014 ± 0.015	0.000	0.192 ± 0.013	0.550	0.210 ± 0.02 ± 0.015	
	0.650	0.098 ± 0.009 ± 0.01	0.000	0.094 ± 0.009	0.650	0.096 ± 0.023 ± 0.01	
35.7	0.150	1.117 ± 0.042 ± 0.03	0.047	1.018 ± 0.038	0.150	0.743 ± 0.042 ± 0.04	0.880 ± 0.029 ± 0.03
	0.250	0.731 ± 0.027 ± 0.02	0.018	0.668 ± 0.024	0.250	0.582 ± 0.031 ± 0.03	
	0.350	0.511 ± 0.021 ± 0.015	0.007	0.470 ± 0.019	0.350	0.474 ± 0.028 ± 0.015	
	0.450	0.328 ± 0.017 ± 0.01	0.003	0.305 ± 0.016	0.450	0.325 ± 0.025 ± 0.01	
	0.550	0.178 ± 0.013 ± 0.01	0.001	0.166 ± 0.012	0.550	0.169 ± 0.020 ± 0.01	
	0.650	0.074 ± 0.008 ± 0.01	0.000	0.070 ± 0.007	0.650	0.071 ± 0.015 ± 0.01	
45.0	0.150	1.039 ± 0.052 ± 0.04	0.060	0.946 ± 0.047	0.150	0.630 ± 0.049 ± 0.05	0.825 ± 0.031 ± 0.03
	0.250	0.809 ± 0.029 ± 0.02	0.025	0.735 ± 0.027	0.250	0.670 ± 0.032 ± 0.02	0.706 ± 0.023 ± 0.02
	0.350	0.497 ± 0.021 ± 0.015	0.010	0.456 ± 0.019	0.350	0.427 ± 0.025 ± 0.015	
	0.450	0.323 ± 0.016 ± 0.01	0.004	0.299 ± 0.015	0.450	0.306 ± 0.021 ± 0.01	
	0.550	0.172 ± 0.012 ± 0.01	0.002	0.160 ± 0.011	0.550	0.184 ± 0.017 ± 0.01	
	0.650	0.073 ± 0.008 ± 0.01	0.001	0.068 ± 0.007	0.650	0.067 ± 0.012 ± 0.01	
56.6	0.150	1.009 ± 0.085 ± 0.04	0.068	0.919 ± 0.078	0.150	0.654 ± 0.078 ± 0.05	0.828 ± 0.042 ± 0.04
	0.250	0.766 ± 0.030 ± 0.02	0.035	0.699 ± 0.027	0.250	0.620 ± 0.030 ± 0.02	0.665 ± 0.024 ± 0.02
	0.350	0.521 ± 0.023 ± 0.015	0.014	0.477 ± 0.021	0.350	0.433 ± 0.026 ± 0.015	0.458 ± 0.020 ± 0.015
	0.450	0.347 ± 0.018 ± 0.015	0.006	0.320 ± 0.017	0.450	0.295 ± 0.022 ± 0.015	
	0.550	0.162 ± 0.012 ± 0.01	0.002	0.150 ± 0.010	0.550	0.173 ± 0.015 ± 0.01	
	0.650	0.085 ± 0.008 ± 0.01	0.001	0.079 ± 0.007	0.650	0.092 ± 0.011 ± 0.01	
71.3	0.150				0.150		0.931 ± 0.064 ± 0.04
	0.250	0.687 ± 0.033 ± 0.02	0.041	0.626 ± 0.030	0.250	0.582 ± 0.031 ± 0.03	0.627 ± 0.026 ± 0.02
	0.350	0.499 ± 0.022 ± 0.015	0.021	0.456 ± 0.020	0.350	0.424 ± 0.023 ± 0.02	0.435 ± 0.018 ± 0.015
	0.450	0.312 ± 0.018 ± 0.015	0.009	0.287 ± 0.016	0.450	0.276 ± 0.020 ± 0.015	0.282 ± 0.016 ± 0.015
	0.550	0.176 ± 0.013 ± 0.015	0.003	0.163 ± 0.012	0.550	0.158 ± 0.015 ± 0.015	0.157 ± 0.011 ± 0.01
	0.650	0.072 ± 0.008 ± 0.01	0.001	0.067 ± 0.007	0.650	0.065 ± 0.009 ± 0.01	
89.7	0.150				0.150		1.014 ± 0.133 ± 0.06
	0.250	0.788 ± 0.063 ± 0.04	0.055	0.718 ± 0.057	0.250	0.712 ± 0.057 ± 0.05	0.685 ± 0.034 ± 0.02
	0.350	0.511 ± 0.026 ± 0.02	0.026	0.466 ± 0.024	0.350	0.407 ± 0.025 ± 0.03	0.433 ± 0.020 ± 0.015
	0.450	0.287 ± 0.017 ± 0.015	0.011	0.263 ± 0.016	0.450	0.265 ± 0.018 ± 0.015	0.257 ± 0.014
	0.550	0.133 ± 0.012 ± 0.015	0.003	0.122 ± 0.011	0.550	0.126 ± 0.013 ± 0.015	0.120 ± 0.010 ± 0.01
	0.650	0.065 ± 0.008 ± 0.01	0.000	0.060 ± 0.007	0.650	0.057 ± 0.009 ± 0.01	0.057 ± 0.007 ± 0.01
113.0	0.250				0.250		0.683 ± 0.051 ± 0.05
	0.350	0.491 ± 0.036 ± 0.03	0.031	0.448 ± 0.033	0.350	0.433 ± 0.033 ± 0.03	0.417 ± 0.023 ± 0.02
	0.450	0.316 ± 0.019 ± 0.02	0.016	0.289 ± 0.017	0.450	0.306 ± 0.018 ± 0.02	0.291 ± 0.016 ± 0.015
	0.550	0.143 ± 0.012 ± 0.015	0.005	0.131 ± 0.011	0.550	0.137 ± 0.012 ± 0.015	0.137 ± 0.010 ± 0.01
	0.650	0.080 ± 0.010 ± 0.01	0.002	0.074 ± 0.009	0.650	0.065 ± 0.010 ± 0.01	0.070 ± 0.007 ± 0.01

Q^2 (GeV^2/c^2)	x	$F_2 \pm \sigma_{stat} \pm \sigma_{syst}$	ΔR	$2xF_1 \pm \sigma_{stat}$	x	$xF_3 \pm \sigma_{stat} \pm \sigma_{syst}$	$F_+ \pm \sigma_{stat} \pm \sigma_{syst}$
142.2	0.250				0.250		0.707 ± 0.126 ± 0.06
	0.350				0.350		0.414 ± 0.031 ± 0.02
	0.450	0.296 ± 0.026 ± 0.02	0.019	0.270 ± 0.024	0.450	0.285 ± 0.024 ± 0.02	0.246 ± 0.017 ± 0.015
	0.550	0.147 ± 0.014 ± 0.02	0.008	0.135 ± 0.013	0.550	0.141 ± 0.013 ± 0.02	0.135 ± 0.011 ± 0.01
	0.650	0.084 ± 0.009 ± 0.01	0.004	0.077 ± 0.009	0.650	0.075 ± 0.009 ± 0.01	0.074 ± 0.007 ± 0.01
179.0	0.350				0.350		0.384 ± 0.058 ± 0.04
	0.450				0.450		0.257 ± 0.023 ± 0.02
	0.550	0.164 ± 0.020 ± 0.02	0.010	0.150 ± 0.019	0.550	0.157 ± 0.018 ± 0.02	0.136 ± 0.013 ± 0.015
	0.650	0.068 ± 0.011 ± 0.01	0.003	0.062 ± 0.010	0.650	0.068 ± 0.010 ± 0.01	0.060 ± 0.007 ± 0.01
225.3	0.450				0.450		0.264 ± 0.044 ± 0.02
	0.550				0.550		0.140 ± 0.018 ± 0.02
	0.650				0.650		0.064 ± 0.011 ± 0.015
283.7	0.550				0.550		0.086 ± 0.033 ± 0.02
	0.650				0.650		0.069 ± 0.014 ± 0.02

Table 5a

Antiquark distribution $\bar{q}^{\bar{\nu}}(x,E_h)$ evaluated assuming $R = \sigma_L/\sigma_T = 0.1$
The estimate of systematic errors is given in Table 5b.

x	E_h	12.6	15.8	19.9	25.1	31.6	39.8	50.1	63.1	79.4	100.0	125.9	158.5
x = 0.015	QBAR	0.123	0.163	0.186	0.266	0.207	0.324	0.331	0.360	0.412	0.425	0.335	0.400
	ERR	0.044	0.019	0.020	0.023	0.023	0.021	0.024	0.028	0.070	0.044	0.048	0.093
	Q_2	0.354	0.446	0.562	0.707	0.890	1.120	1.410	1.776	2.235	2.814	3.543	4.460
	ΔR	0.018	0.016	0.015	0.016	0.012	0.018	0.021	0.018	0.029	0.019	0.013	0.017
x = 0.045	QBAR	0.214	0.219	0.276	0.317	0.286	0.327	0.374	0.391	0.290	0.407	0.319	0.364
	ERR	0.076	0.030	0.032	0.038	0.032	0.029	0.030	0.037	0.081	0.057	0.061	0.071
	Q_2	1.063	1.338	1.684	2.121	2.670	3.361	4.231	5.327	6.706	8.442	10.628	13.380
	ΔR	0.034	0.027	0.027	0.031	0.019	0.028	0.028	0.030	0.040	0.032	0.022	0.014
x = 0.08	QBAR	0.180	0.230	0.230	0.241	0.262	0.289	0.323	0.280	0.381	0.343	0.252	0.278
	ERR	0.074	0.029	0.029	0.031	0.032	0.024	0.025	0.028	0.068	0.046	0.039	0.052
	Q_2	1.889	2.995	2.995	3.770	4.746	5.975	7.522	9.469	11.921	15.008	18.894	23.786
	ΔR	0.042	0.031	0.031	0.031	0.025	0.028	0.029	0.028	0.034	0.030	0.018	0.013
x = 0.125	QBAR	0.161	0.181	0.209	0.151	0.174	0.195	0.211	0.182	0.251	0.198	0.205	0.167
	ERR	0.072	0.028	0.027	0.031	0.025	0.019	0.020	0.023	0.066	0.028	0.036	0.055
	Q_2	2.952	3.717	4.679	5.890	7.416	9.336	11.753	14.796	18.627	23.450	29.522	37.166
	ΔR	0.046	0.033	0.030	0.033	0.023	0.025	0.026	0.026	0.041	0.020	0.023	0.021
x = 0.175	QBAR	0.138	0.103	0.118	0.129	0.104	0.101	0.123	0.146	0.146	0.147	0.153	0.124
	σ_{stat}	0.057	0.027	0.026	0.028	0.021	0.018	0.019	0.022	0.047	0.031	0.036	0.034
	Q_2	4.133	5.203	6.550	8.247	10.381	13.070	16.454	20.714	26.078	32.830	41.331	52.032
	ΔR	0.034	0.031	0.029	0.030	0.017	0.023	0.025	0.026	0.028	0.025	0.023	0.009
x = 0.225	QBAR	0.015	0.073	0.060	0.087	0.077	0.076	0.078	0.063	0.046	0.043	0.042	0.052
	ERR	0.081	0.024	0.026	0.027	0.020	0.018	0.015	0.018	0.037	0.015	0.018	0.022
	Q_2	5.314	6.690	8.422	10.603	13.348	16.804	21.155	26.633	33.529	42.210	53.139	66.898
	ΔR	0.046	0.027	0.027	0.026	0.017	0.022	0.019	0.021	0.024	0.011	0.011	0.008
x = 0.275	QBAR	0.052	0.028	0.054	0.049	0.078	0.044	0.040	0.031	0.013	0.043	-0.004	0.034
	ERR	0.062	0.023	0.021	0.021	0.019	0.015	0.014	0.014	0.033	0.019	0.018	0.031
	Q_2	6.495	8.177	10.294	12.959	16.314	20.538	25.856	32.551	40.979	51.590	64.948	81.765
	ΔR	0.031	0.021	0.019	0.018	0.015	0.017	0.017	0.016	0.019	0.013	0.014	0.010
x = 0.35	QBAR	-0.039	0.019	0.026	0.009	0.005	0.011	0.004	0.019	-0.007	0.013	0.014	0.010
	ERR	0.038	0.013	0.013	0.014	0.010	0.008	0.008	0.008	0.019	0.011	0.006	0.007
	Q_2	8.266	10.406	13.101	16.493	20.764	26.140	32.908	41.429	52.156	65.660	82.661	104.064
	ΔR	0.024	0.016	0.015	0.006	0.009	0.013	0.012	0.011	0.014	0.010	0.006	0.004
x = 0.45	QBAR	0.003	-0.006	-0.002	-0.007	0.002	-0.006	-0.002	-0.002	-0.016	0.007	-0.008	0.000
	ERR	0.029	0.011	0.009	0.012	0.007	0.007	0.005	0.005	0.013	0.008	0.013	0.000
	Q_2	10.628	13.380	16.844	21.205	26.696	33.608	42.310	53.265	67.057	86.500	106.279	0.000
	ΔR	0.013	0.010	0.009	0.010	0.006	0.009	0.007	0.006	0.008	0.005	0.007	0.000
x = 0.60	QBAR	-0.009	-0.002	-0.002	0.001	-0.001	-0.001	-0.001	0.001	0.002	0.002	-0.001	0.002
	ERR	0.010	0.003	0.003	0.003	0.002	0.002	0.001	0.001	0.003	0.003	0.003	0.003
	Q_2	14.171	17.840	22.459	28.274	35.595	44.811	56.414	71.021	89.410	116.220	141.705	178.396
	ΔR	0.005	0.003	0.002	0.002	0.001	0.002	0.001	0.001	0.001	0.001	0.001	0.001

Row 1 (QBAR): Value of structure function
Row 2 (ERR) : Statistical error on $\bar{q}^{\bar{\nu}}$
Row 3 (Q_2) : Value of Q_2 corresponding to centre of bin
Row 4 (ΔR) : Effect of Callan-Gross violation $\Delta R = \bar{q}(R = 0.0) - \bar{q}(R = 0.1)$

Table 5b

The structure function $\bar{q}^{\bar{\nu}}(x,Q^2)$ evaluated under the assumption $R = \sigma_L/\sigma_T = 0.1$.
Statistical and systematic point-to-point errors are given separately.
In addition, $\bar{q}^{\bar{\nu}}$ has an over-all scale error of ±8%.

Q^2 (GeV^2/c^2)	x	$\bar{q}^{\bar{\nu}} \pm \sigma_{stat} \pm \sigma_{syst}$
0.450	0.015	0.146 ± 0.028 ± 0.03
0.566	0.015	0.195 ± 0.033 ± 0.03
0.713	0.015	0.300 ± 0.035 ± 0.03
0.897	0.015	0.311 ± 0.037 ± 0.02
	0.045	0.431 ± 0.151 ± 0.08
1.13	0.015	0.323 ± 0.041 ± 0.02
	0.015	0.248 ± 0.074 ± 0.08
1.42	0.015	0.339 ± 0.038 ± 0.02
	0.045	0.252 ± 0.046 ± 0.05
1.79	0.015	0.348 ± 0.035 ± 0.02
	0.045	0.241 ± 0.038 ± 0.02
	0.08	0.281 ± 0.178 ± 0.06
2.25	0.015	0.307 ± 0.037 ± 0.02
	0.045	0.271 ± 0.036 ± 0.02
	0.08	0.182 ± 0.066 ± 0.05
2.84	0.015	0.438 ± 0.058 ± 0.02
	0.045	0.357 ± 0.038 ± 0.02
	0.08	0.212 ± 0.040 ± 0.03
	0.15	0.236 ± 0.142
3.57	0.015	0.456 ± 0.067 ± 0.02
	0.045	0.370 ± 0.034 ± 0.02
	0.08	0.238 ± 0.034 ± 0.02
	0.15	0.111 ± 0.062 ± 0.02
4.50	0.015	0.472 ± 0.089 ± 0.03
	0.045	0.395 ± 0.034 ± 0.02
	0.08	0.251 ± 0.030 ± 0.02
	0.15	0.179 ± 0.028 ± 0.02
5.66	0.015	0.259 ± 0.082 ± 0.05
	0.045	0.342 ± 0.035 ± 0.02
	0.08	0.288 ± 0.026 ± 0.02
	0.15	0.174 ± 0.022 ± 0.02
	0.25	0.012 ± 0.113 ± 0.02
7.13	0.045	0.269 ± 0.034 ± 0.02
	0.08	0.278 ± 0.025 ± 0.02
	0.15	0.153 ± 0.021 ± 0.01
	0.25	0.064 ± 0.037 ± 0.02
8.97	0.045	0.284 ± 0.057 ± 0.03
	0.08	0.297 ± 0.027 ± 0.02
	0.15	0.141 ± 0.016 ± 0.01
	0.25	0.045 ± 0.021 ± 0.01
	0.35	-0.047 ± 0.047 ± 0.03
11.30	0.045	0.343 ± 0.066 ± 0.04
	0.08	0.292 ± 0.030 ± 0.02
	0.15	0.179 ± 0.016 ± 0.01
	0.25	0.051 ± 0.018 ± 0.01
	0.35	0.019 ± 0.021 ± 0.01
	0.45	-0.037 ± 0.051 ± 0.01

Q^2 (GeV^2/c^2)	x	$\bar{q}^{\bar{\nu}} \pm \sigma_{stat} \pm \sigma_{syst}$
14.22	0.045	0.417 ± 0.104 ± 0.05
	0.08	0.284 ± 0.038 ± 0.02
	0.15	0.143 ± 0.014 ± 0.01
	0.25	0.070 ± 0.014 ± 0.005
	0.35	0.022 ± 0.015 ± 0.01
	0.45	0.013 ± 0.015 ± 0.01
	0.55	-0.006 ± 0.042 ± 0.01
17.90	0.08	0.346 ± 0.051 ± 0.03
	0.15	0.165 ± 0.015 ± 0.01
	0.25	0.058 ± 0.011 ± 0.005
	0.35	0.030 ± 0.013 ± 0.005
	0.45	-0.007 ± 0.012 ± 0.005
	0.55	-0.013 ± 0.014 ± 0.005
22.54	0.08	0.166 ± 0.047 ± 0.05
	0.15	0.125 ± 0.017 ± 0.01
	0.25	0.065 ± 0.010 ± 0.005
	0.35	0.015 ± 0.009 ± 0.005
	0.45	-0.001 ± 0.010 ± 0.003
	0.55	-0.007 ± 0.008 ± 0.003
28.37	0.15	0.152 ± 0.024 ± 0.02
	0.25	0.077 ± 0.011 ± 0.005
	0.35	0.017 ± 0.008 ± 0.005
	0.45	0.004 ± 0.007 ± 0.003
	0.55	-0.008 ± 0.007 ± 0.003
35.72	0.15	0.174 ± 0.027 ± 0.03
	0.25	0.055 ± 0.012 ± 0.005
	0.35	0.013 ± 0.007 ± 0.003
	0.45	-0.002 ± 0.005 ± 0.003
	0.55	-0.000 ± 0.005 ± 0.003
44.96	0.25	0.044 ± 0.013 ± 0.005
	0.35	0.010 ± 0.007 ± 0.003
	0.45	0.006 ± 0.005 ± 0.002
	0.55	0.001 ± 0.005 ± 0.002
56.61	0.25	0.042 ± 0.014 ± 0.005
	0.35	0.005 ± 0.006 ± 0.003
	0.45	0.004 ± 0.005 ± 0.002
	0.55	0.001 ± 0.005 ± 0.002
71.26	0.25	0.011 ± 0.012 ± 0.01
	0.35	0.011 ± 0.007 ± 0.003
	0.45	0.002 ± 0.008 ± 0.002
	0.55	-0.002 ± 0.005 ± 0.002
89.72	0.35	0.034 ± 0.013 ± 0.006
	0.45	-0.003 ± 0.007 ± 0.003
	0.55	0.001 ± 0.004 ± 0.003
112.9	0.35	0.015 ± 0.014 ± 0.01
	0.45	-0.003 ± 0.005 ± 0.003
	0.55	-0.000 ± 0.008 ± 0.003
142.2	0.45	-0.002 ± 0.007 ± 0.004
	0.55	-0.002 ± 0.003 ± 0.003

Table 6

Dependence of F_2 on the magnitude of the strange- and charmed-sea correction. The ratio of F_2 for the two values $2(s-c)/(\bar{u}+\bar{d}) = 0.4$ and $2(s-c)/(\bar{u}+\bar{d}) = 0.2$ is given as a function of x and Q^2

Q^2 \ x	0.015	0.045	0.08	0.15	0.25	0.35
1.4	0.95	0.98	0.99	1	1	
3.5	0.93	0.96	0.98	0.99	1	
9.0		0.95	0.96	0.97	0.99	1
18			0.95	0.97	0.99	1
36				0.97	0.99	1
72					0.99	1

Table 7

Results of QCD fits to the structure function measurements with $Q^2 > 2\ GeV^2/c^2$ and $W^2 > 11\ GeV^2$. The errors on Λ are statistical only

Structure function	Λ (GeV)	$F_i(x,Q_0^2)$	x^2/DF
F_{NS} $(x > 0.03)$ $R = R_{QCD}$	$\Lambda_{LO} = 0.275 \pm 0.08$ $\Lambda_{\overline{MS}} = 0.30 \pm 0.08$	$F_{NS} = \frac{3}{B} x^{0.374}(1-x)^{3.31}(1+5.86x)$	48/49
F_2 and $\bar{q}^{\bar{\nu}}$ all x $R = 0.1$	$\Lambda_{LO} = 0.18 \pm 0.02$	$F_2 = 1.10(1+3.7x)(1-x)^{3.19}$ $\bar{q}^{\bar{\nu}} = 0.52(1-x)^{8.54}$ $G = 2.62(1+3.5x)(1-x)^{5.90}$ $Q_0^2 = 5\ GeV^2/c^2$	209/196
F_2 $(x > 0.03)$ $\bar{q}^{\bar{\nu}}$ $(x > 0.3)$ $R = R_{QCD}$ Corrected for slow rescaling	$\Lambda_{LO} = 0.29 \pm 0.03$	$F_2 = 1.18(1+3.27x)(1-x)^{3.12}$ $\bar{q}^{\bar{\nu}} = 0.53(1-x)^{7.12}$ $G = 1.75(1+8.9x)(1-x)^{6.03}$ $Q_0^2 = 5\ GeV^2/c^2$	136/130

Table 8

Systematic dependences of Λ_{LO} for the QCD fit to F_{NS} ($x > 0.3$ and $W^2 > 11$ GeV^2)

Fit	Λ_{LO} (GeV)	χ^2/DF
Standard fit $R = R_{QCD}$	0.275 ± 0.09	48/49
$R = 0.0$	0.295	47.9/49
$R = 0.1$	0.21	53/49
$R = 0.2$	0.10	58.4/49
$m_W = \infty$	0.37	48/49
No target mass correction	0.28	48/49
No sea quark correction	0.21	49/49

Figure captions

Fig. 1 : Over-all view of the detector.

Fig. 2 : Fiducial region of the calorimeter modules. The central region inside the lozenge-shaped area has been excluded from the analysis.

Fig. 3 : Absolute neutrino flux as a function of energy for the narrow-band and wide-band beams in which the present data have been obtained:
a) neutrino beams,
b) antineutrino beams.

Fig. 4 : Computer reconstruction of a charged-current neutrino interaction in the detector. The neutrino enters from the left. The top row gives the pulse height in the scintillator planes along the detector. The rows below show the measured coordinates in the three drift-chamber projections together with the fit curve for the muon reconstruction.

Fig. 5 : a) Acceptance of the detector for charged-current events as a function of y for five different bins in x for neutrinos from the decay of 300 GeV/c kaons.
b) Resolution of the detector in the scaling variable x for three ranges in Q^2.

Fig. 6 : Energy dependence of the total neutrino and antineutrino cross-sections. The error bars include an estimate of systematic point-to-point errors. The solid line shows the energy dependence as expected from the observed scaling violation of the structure functions. The dashed lines indicate the over-all scale errors.

Fig. 7 : $R = \sigma_L/\sigma_T$ averaged over x as a function of the energy transfer. The inner error bars are the statistical errors, the full error bars include an estimate of the systematic errors.

Fig. 8 : $R = \sigma_L/\sigma_T$ averaged over ν as a function of x compared with the leading-order QCD prediction with $\Lambda = 0.2$ GeV. Also shown is the average value of Q^2 for each bin in x. The inner error bars are the statistical errors, the full error bars include an estimate of the systematic errors. The data points with arrow are upper limits on R.

Fig. 9 : $R = \sigma_L/\sigma_T$ as a function of x for the present experiment compared with measurements in ep, ed [20], and μN [21] scattering. For the SLAC electron data, only statistical errors are given. The curve is the QCD prediction for the kinematic range of this experiment neglecting the contribution of the charmed quark.

Fig. 10 : Structure function F_2 versus Q^2 for different bins in x. The solid lines are the result of a leading-order QCD fit to F_2 and $\bar{q}^{\bar{\nu}}$.

Fig. 11 : The structure function xF_3 versus Q^2 for different bins in x. The dashed lines are the result of a leading-order QCD fit to the data.

Fig. 12 : The structure function F_+ versus Q^2 for different bins in x.

Fig. 13 : The differential antineutrino cross-section as a function of x for four bins in y and two neutrino energies. Also shown is the neutrino cross-section multiplied by $(1-y)^2$. The curves are parametrizations of the data which have been used in the Monte Carlo simulation to determine the unsmearing corections.

Fig. 14 : The structure function $\bar{q}^{\bar{\nu}}$ versus Q^2 for different bins in x. The solid lines are the result of a QCD fit to F_2 and $\bar{q}^{\bar{\nu}}$.

Fig. 15 : Comparison of the structure functions $2xF_1$, F_+, xF_3, and $\bar{q}^{\bar{\nu}}$ for fixed Q^2 as a function of x. The curves are empirical fits to the data which fulfil the quark parton model relations between these structure functions: $2xF_1 = q + \bar{q}$, $xF_3 = q - \bar{q}$, $F_+ = q + xs$, $\bar{q}^{\bar{\nu}} = \bar{q} + xs$ with $2s/\bar{q} = 0.4$.

Fig. 16 : The x-dependence of the strange sea as measured by $\sim$ 2000 opposite sign dimuon events from antineutrino interactions. The solid curve is a parametrization of $\bar{q}^{\bar{\nu}} = x(\bar{u}+\bar{d}+2\bar{s})$. The dashed curve includes the effect of the charm mass threshold effect with an effective charm mass of 1.5 GeV as calculated in the slow rescaling model. The curves are normalized to the observed event numbers.

Fig. 17 : a) The structure functions F_2, xF_3, and $\bar{q}^{\bar{\nu}}$ as measured in this experiment for fixed Q^2 as a function of x. The data on F_2 are compared with the measurements of $F_2^{\mu N}$ by EMC [24] and of F_2^{ed} by SLAC-MIT [20] multiplied by the quark parton model factors.

b) The Q^2 dependence of the structure function F_2 versus x as measured by this experiment compared with the results of the EMC muon experiment [24]. The data points are obtained by linear fits of ln F_2 versus ln Q^2 in the whole Q^2 range of the experiments. The solid line gives the QCD expectation for Λ = 0.2 GeV.

Fig. 18 : a) The slopes $dF_2/d \ln Q^2$ for the structure function $F_2^{\nu N}$ as obtained by linear fits to the data in ln ln Q^2 extrapolated to $Q^2 = 4.5$ GeV$^2/c^2$. The solid line is the result of a leading-order QCD fit to F_2 and $\bar{q}^{\bar{\nu}}$. The dashed lines correspond to predictions for non-asymptotically free theories of the strong interaction with scalar and vector gluons.

b) The slopes $d\bar{q}^{\bar{\nu}}/d \ln Q^2$ for the structure function $\bar{q}^{\bar{\nu}}$ at $Q^2 = 4.5$ GeV$^2/c^2$. The solid line is the prediction of a QCD fit to F_2 and $\bar{q}^{\bar{\nu}}$. The dashed lines show the separate contributions due to gluon bremsstrahlung and quark pair production.

Fig. 19 : The structure functions F_2, $\bar{q}^{\bar{\nu}}$, and G(x) for fixed Q^2 as obtained from the QCD fit to F_2 and $\bar{q}^{\bar{\nu}}$. Also shown are the $\pm 1\sigma$ bands for G(x) and the measurements of F_2 and $\bar{q}^{\bar{\nu}}$ projected to $Q^2 = 4.5$ GeV$^2/c^2$ along the QCD fit lines.

Fig. 20 : The slopes $dF_2/d \ln Q^2$ for the structure function $F_2^{\nu N}$ as obtained from linear fits to the data in $\ln \ln Q^2$ at fixed Q^2 and two assumptions about $R = \sigma_L/\sigma_T$. The solid curve indicates the scaling violations due to the charm threshold effect in the transition $s \to c$ as estimated by the slow rescaling model.

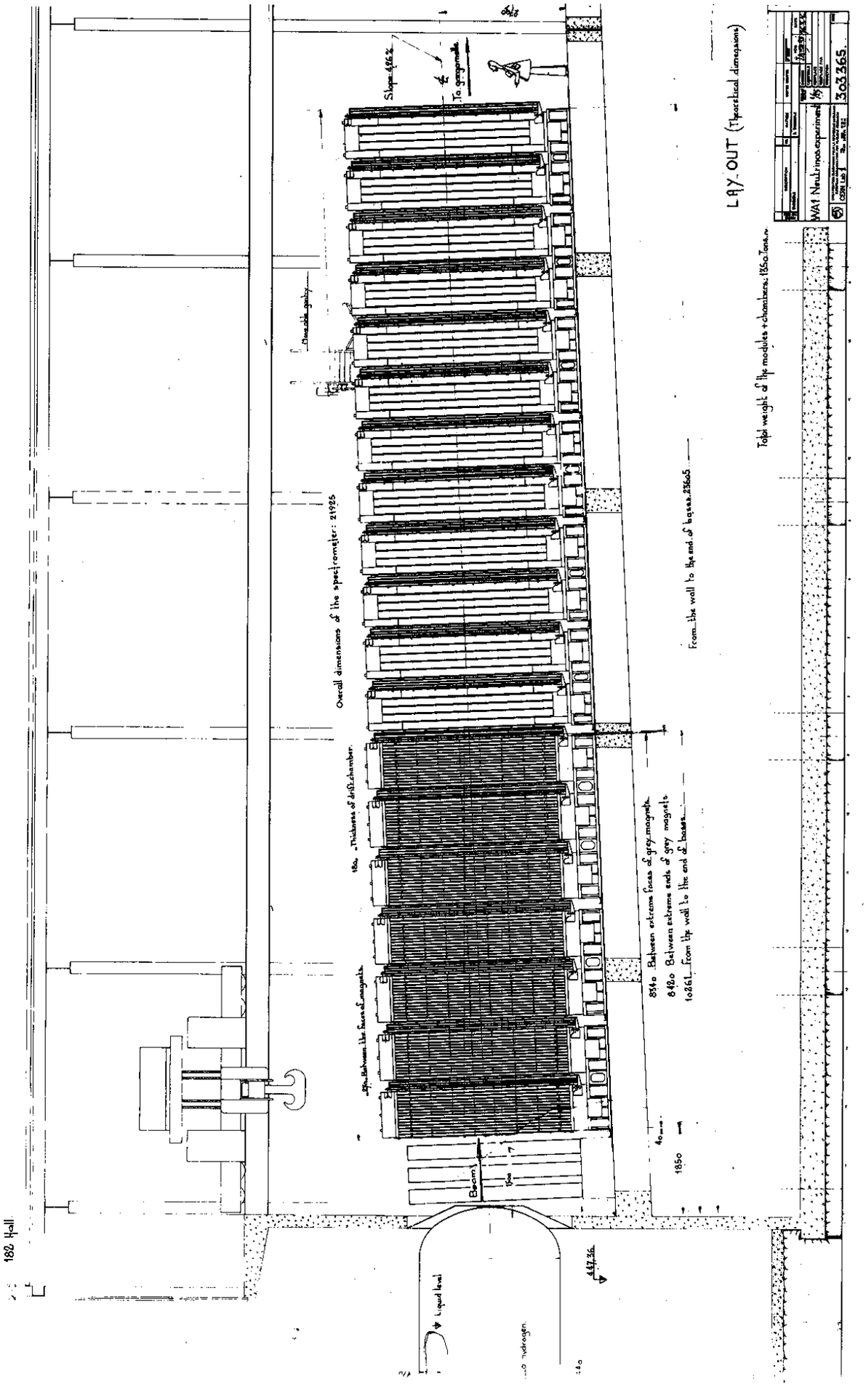
182 Hall
Liquid level
Hydrogen
Beam
Overall dimensions of the spectrometer: 21925
Thickness of drift chamber
Between the faces of magnets
Between extreme faces of grey magnets
Between extreme ends of grey magnets
From the wall to the end of bases
From the wall to the end of bases 23605
LAY-OUT (Theoretical dimensions)
Total weight of the modules + chambers: 1850 tons
Slope 4.8%
To garganella
WA1 Neutrinos experiment
303365

Fig. 1

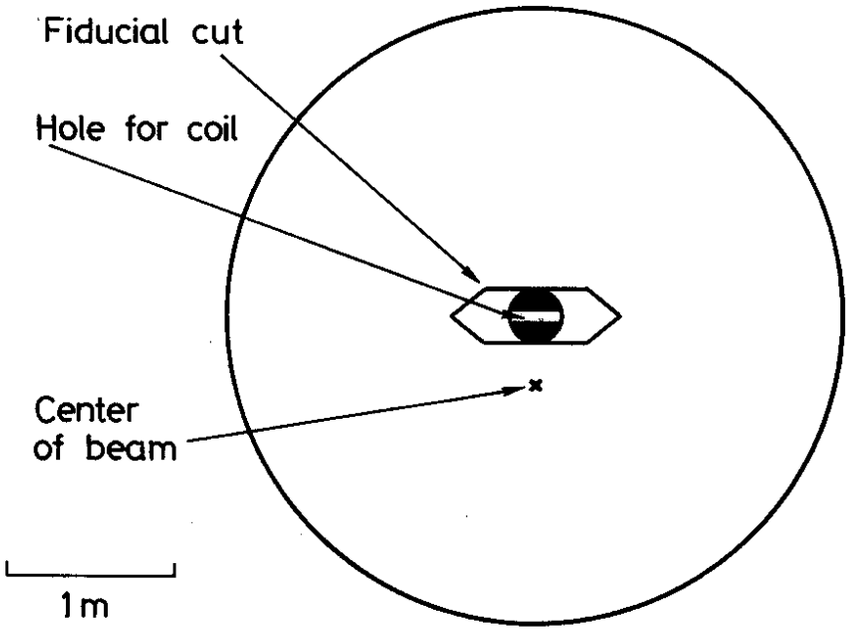

Fig. 2

a)

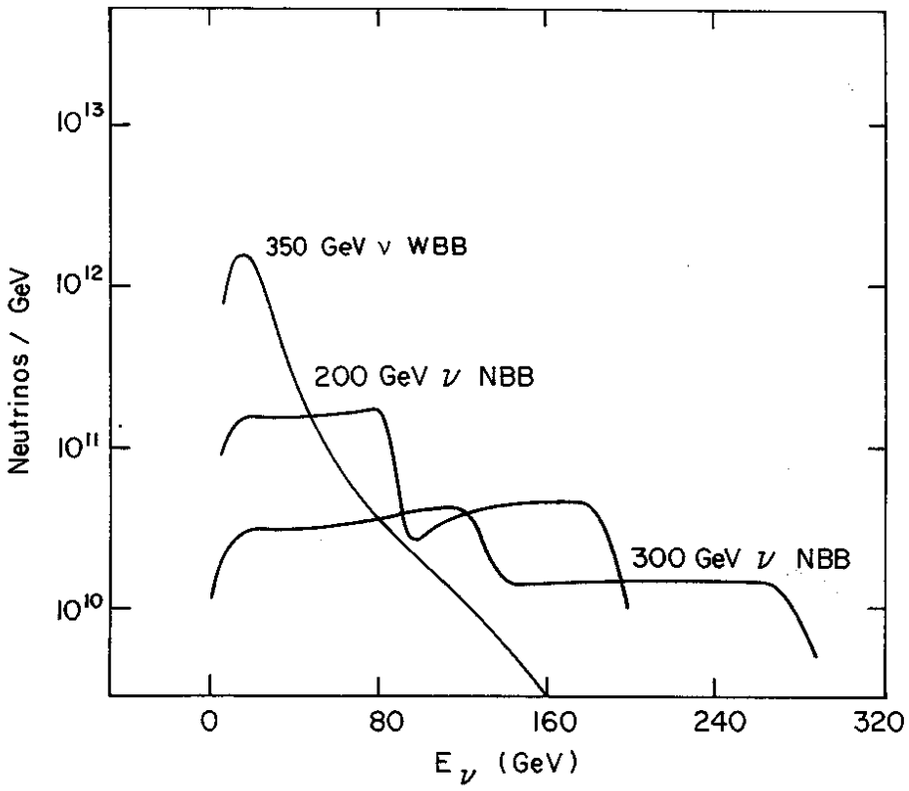
Neutrinos / GeV
10^{13}
10^{12}
10^{11}
10^{10}
350 GeV ν WBB
200 GeV ν NBB
300 GeV ν NBB
0
80
160
240
320
E_ν (GeV)

b)

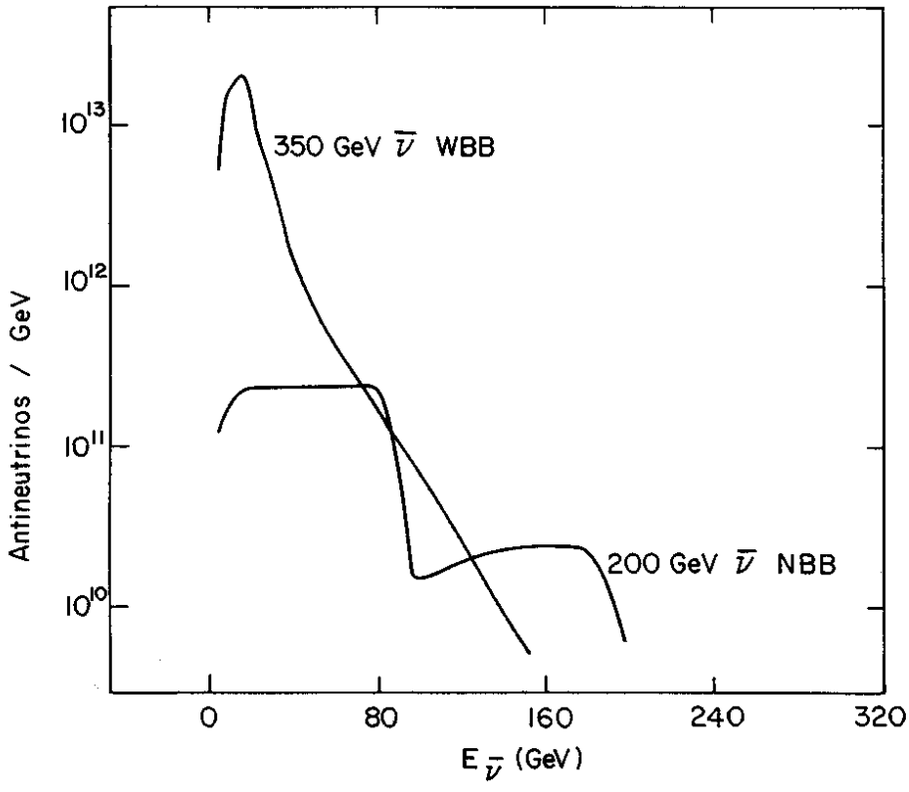
Antineutrinos / GeV
10^{13}
10^{12}
10^{11}
10^{10}
350 GeV $\bar{\nu}$ WBB
200 GeV $\bar{\nu}$ NBB
0
80
160
240
320
$E_{\bar{\nu}}$ (GeV)

Fig. 3

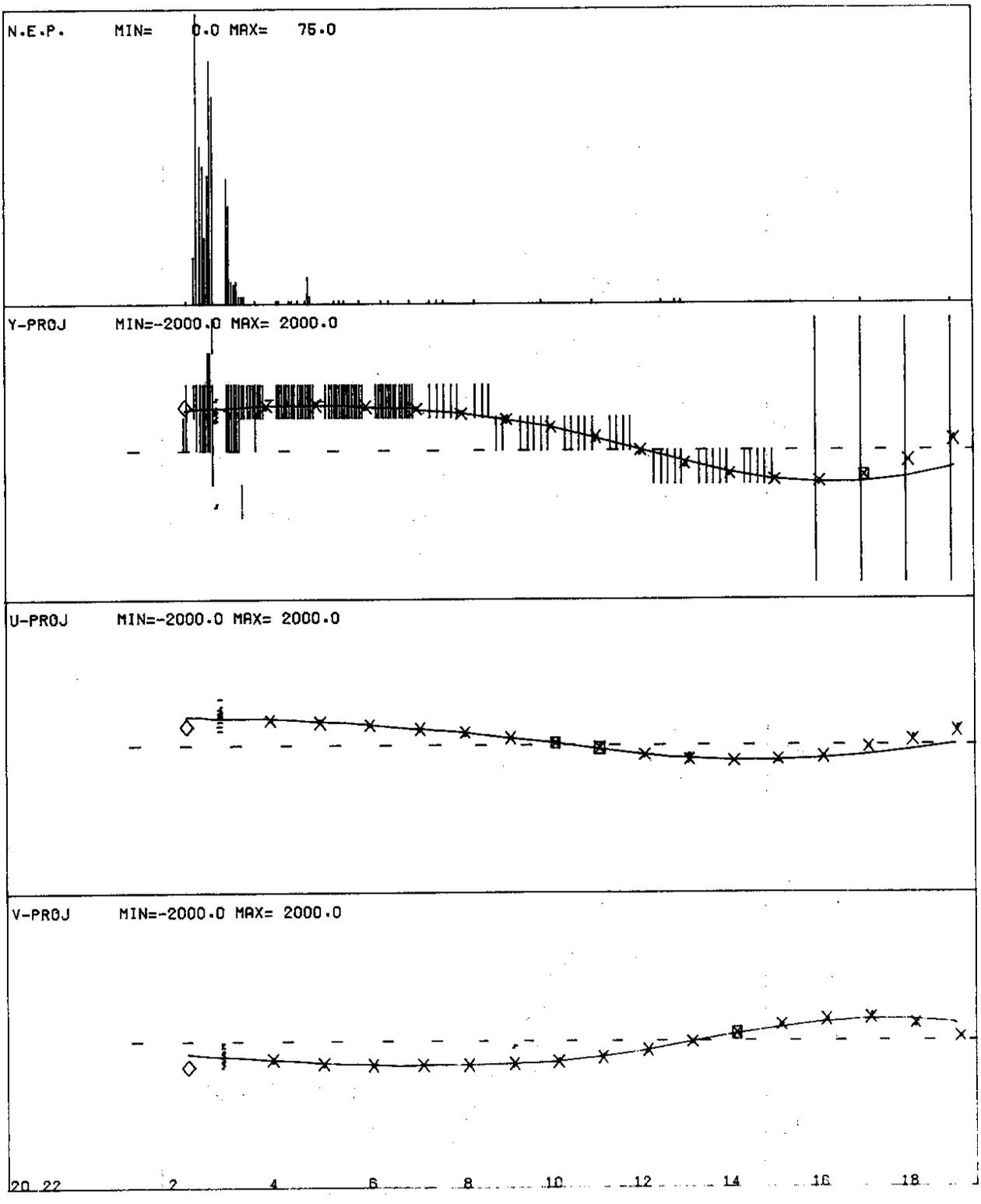
N.E.P. MIN= 0.0 MAX= 75.0
Y-PROJ MIN=-2000.0 MAX= 2000.0
U-PROJ MIN=-2000.0 MAX= 2000.0
V-PROJ MIN=-2000.0 MAX= 2000.0
20 22 2 4 6 8 10 12 14 16 18

Fig. 4

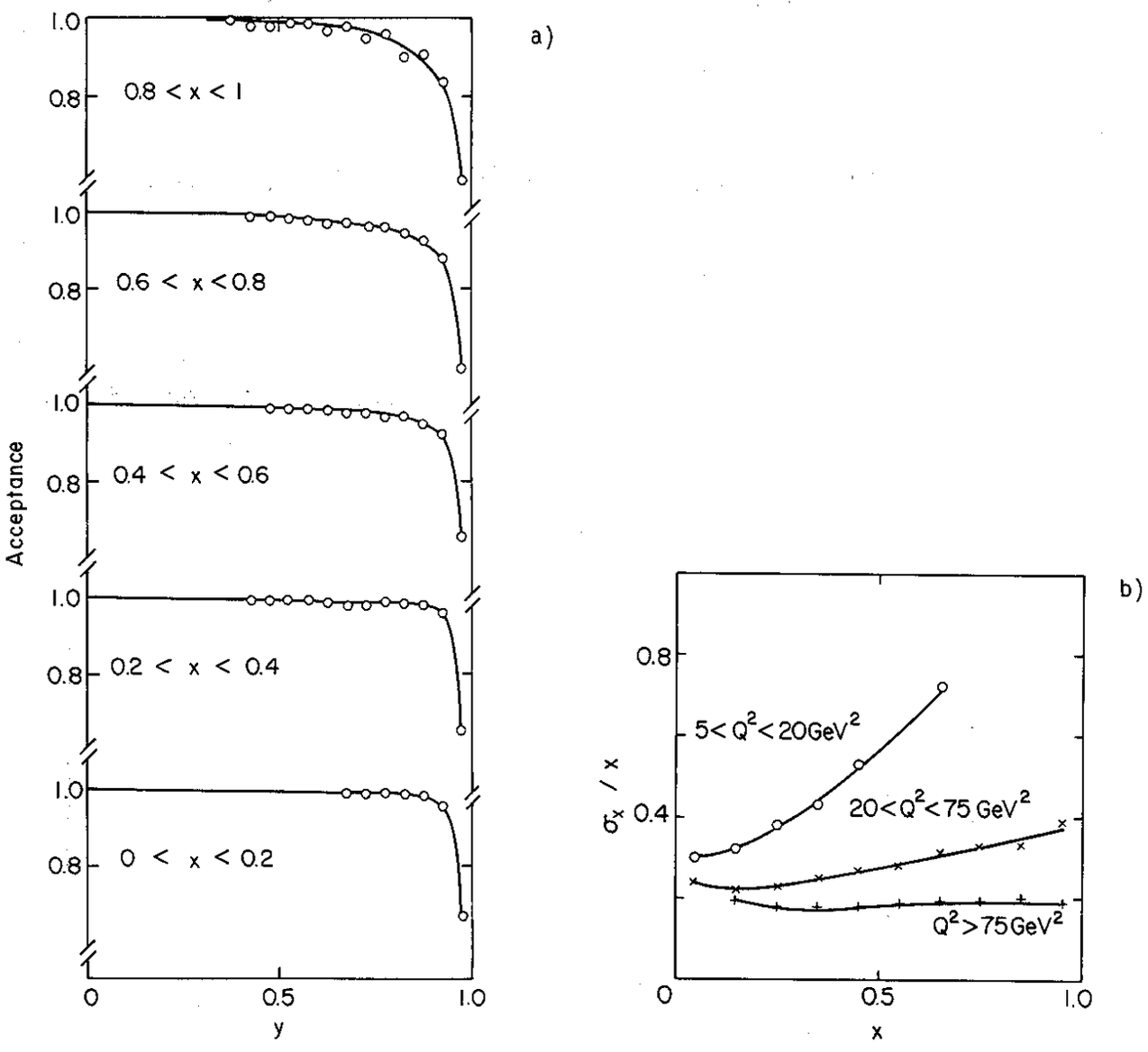
a)
Acceptance
1.0
0.8
0.8 < x < 1
0.6 < x < 0.8
0.4 < x < 0.6
0.2 < x < 0.4
0 < x < 0.2
0
0.5
1.0
y
b)
σ_x / x
0.8
0.4
0
$5<Q^2<20GeV^2$
$20<Q^2<75\,GeV^2$
$Q^2>75GeV^2$
0.5
1.0
x

Fig. 5

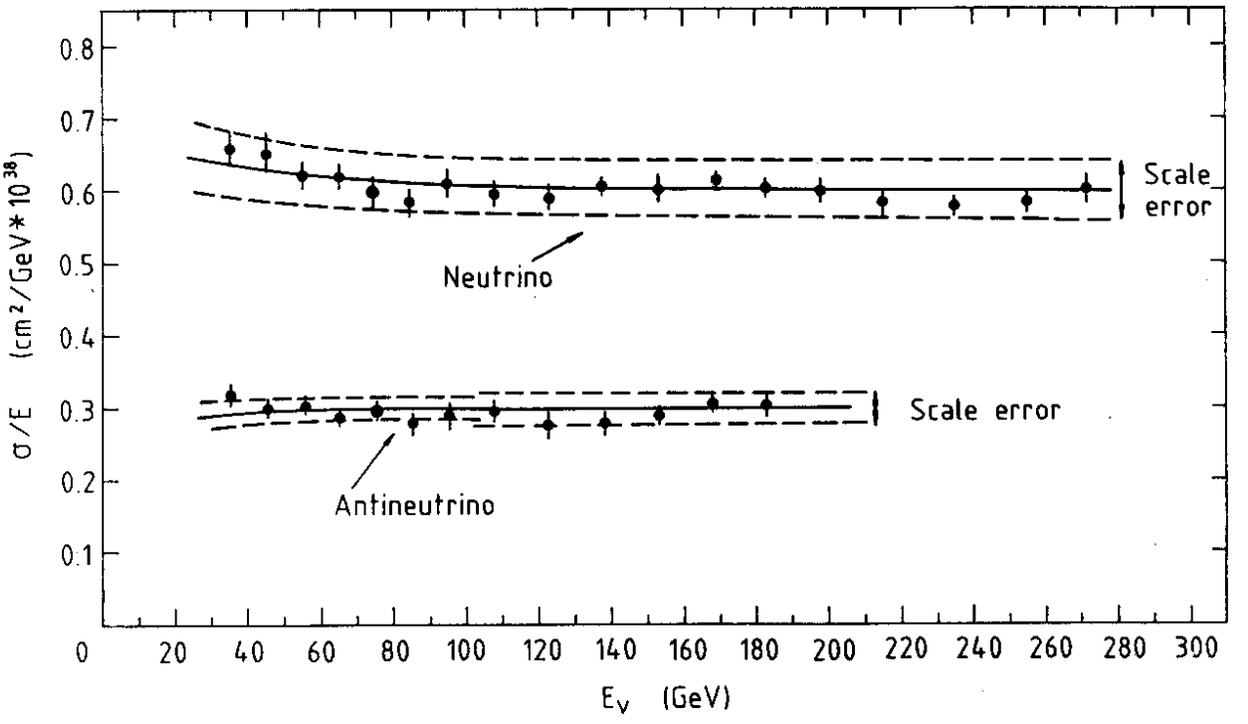
σ/E (cm²/GeV*10⁻³⁸)
Neutrino
Scale error
Antineutrino
Scale error
E_ν (GeV)

Fig. 6

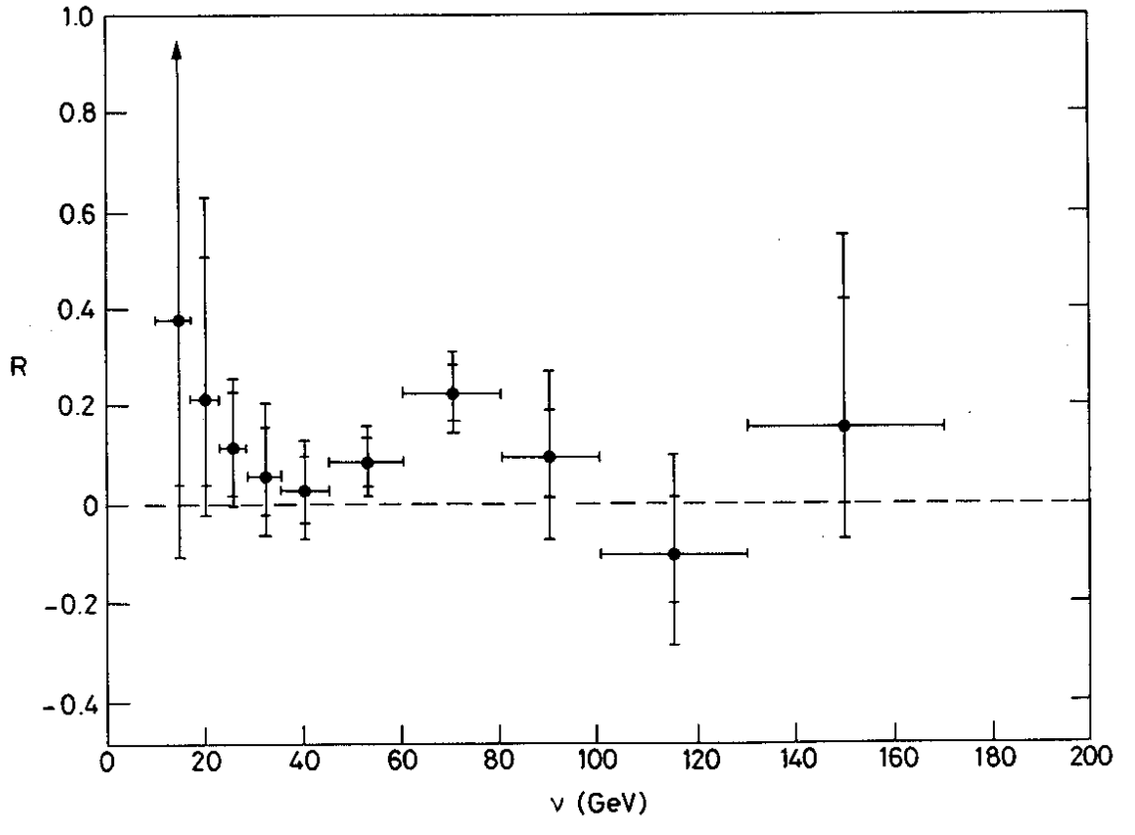
R
ν (GeV)

Fig. 7

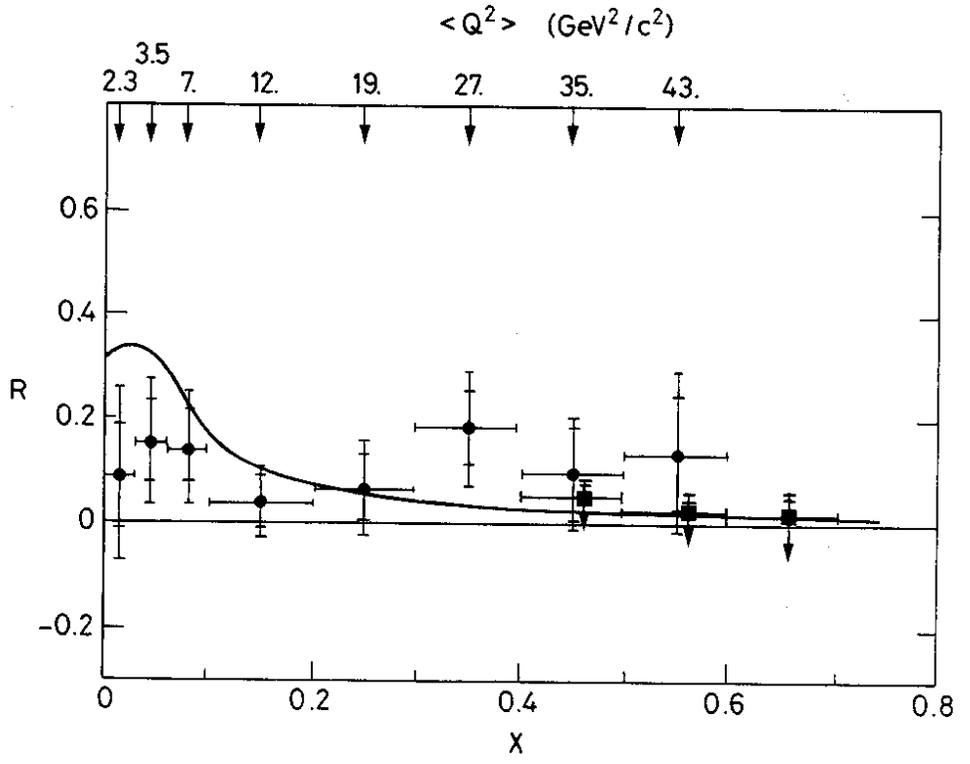
$<Q^2>$ (GeV^2/c^2)
2.3
3.5
7.
12.
19.
27.
35.
43.
R
X
0.6
0.4
0.2
0
-0.2
0
0.2
0.4
0.6
0.8

Fig. 8

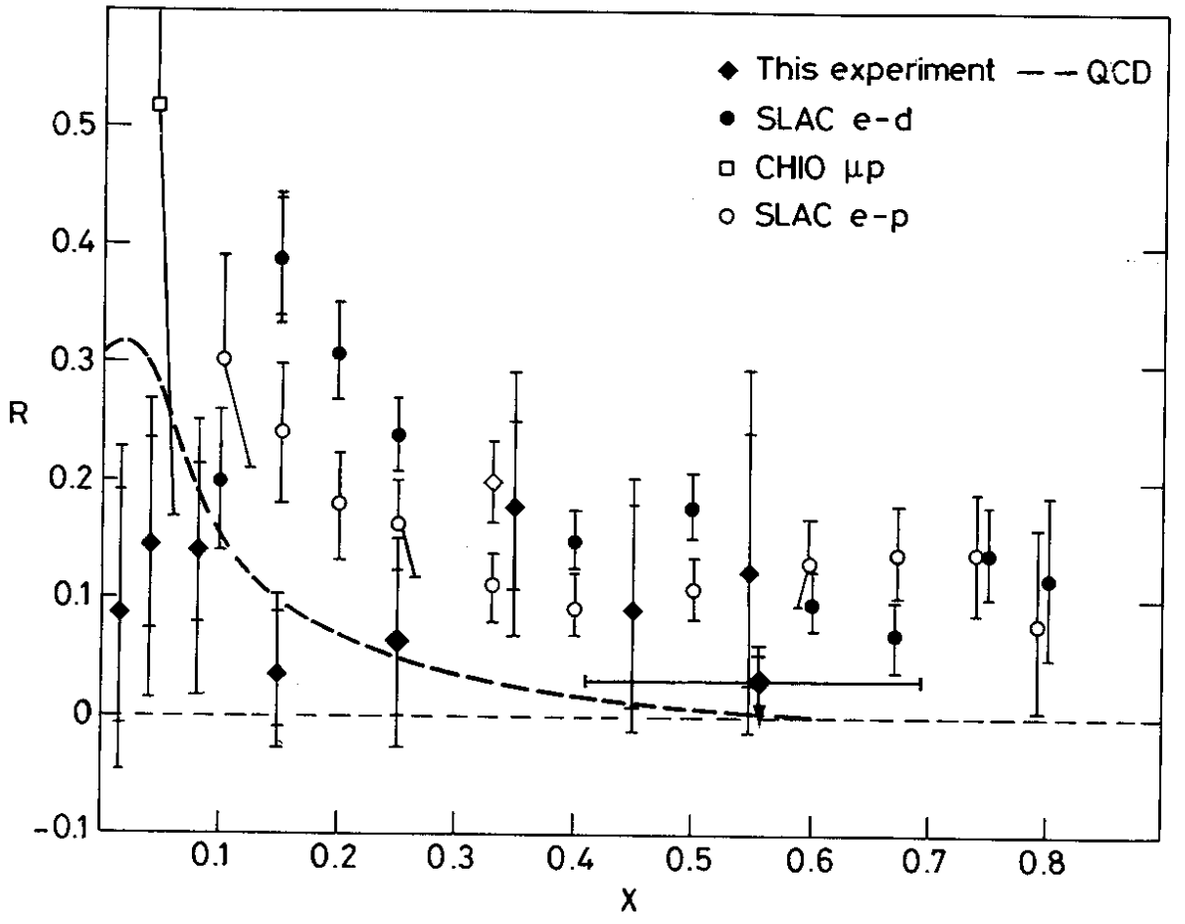
This experiment
QCD
SLAC e-d
CHIO μp
SLAC e-p
R
X
0.5
0.4
0.3
0.2
0.1
0
-0.1
0.1
0.2
0.3
0.4
0.5
0.6
0.7
0.8

Fig. 9

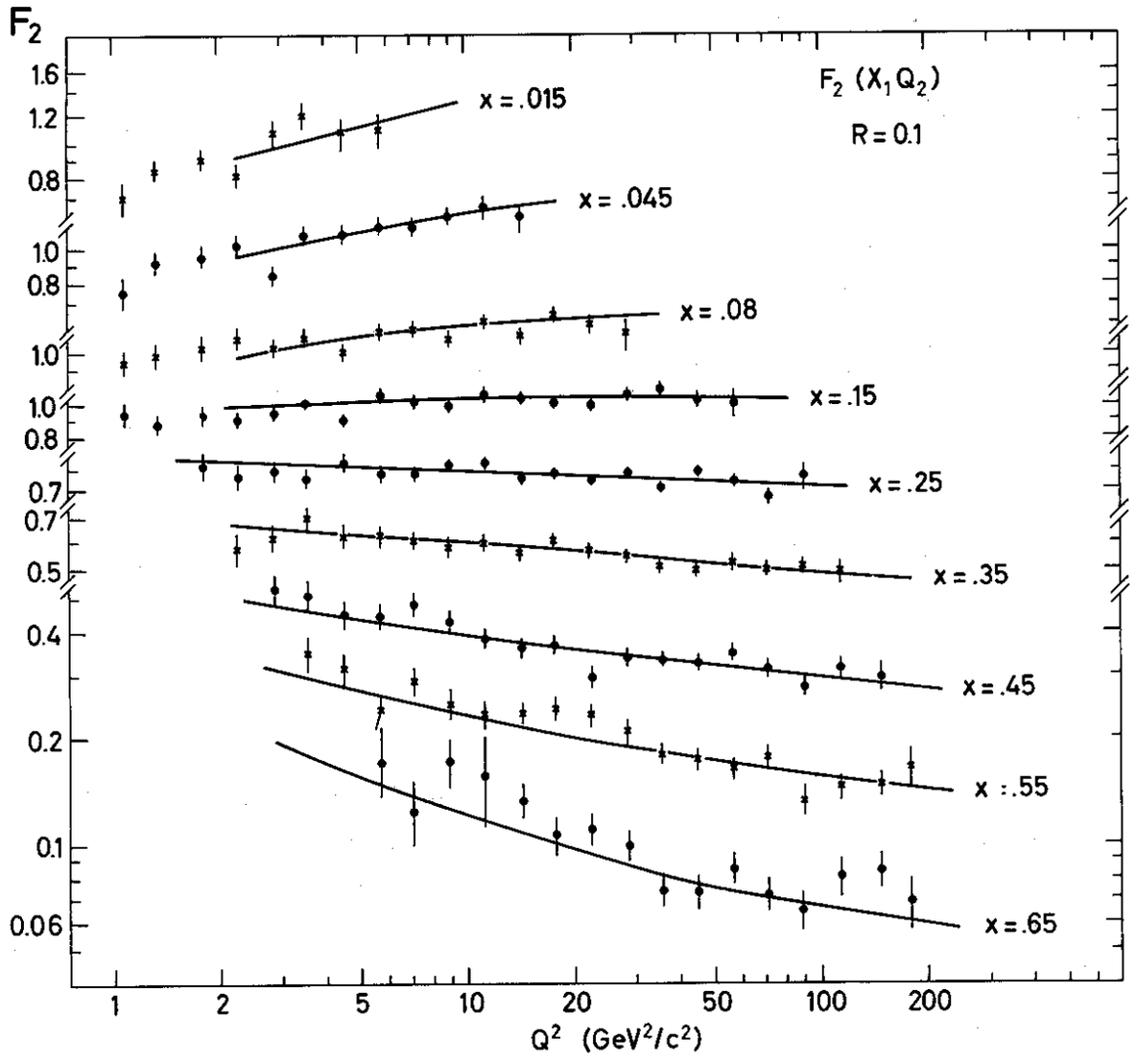
F2
F2 (X1 Q2)
R = 0.1
x = .015
x = .045
x = .08
x = .15
x = .25
x = .35
x = .45
x = .55
x = .65
1.6
1.2
0.8
1.0
0.8
1.0
1.0
0.8
0.7
0.7
0.5
0.4
0.2
0.1
0.06
1
2
5
10
20
50
100
200
Q2 (GeV2/c2)

Fig. 10

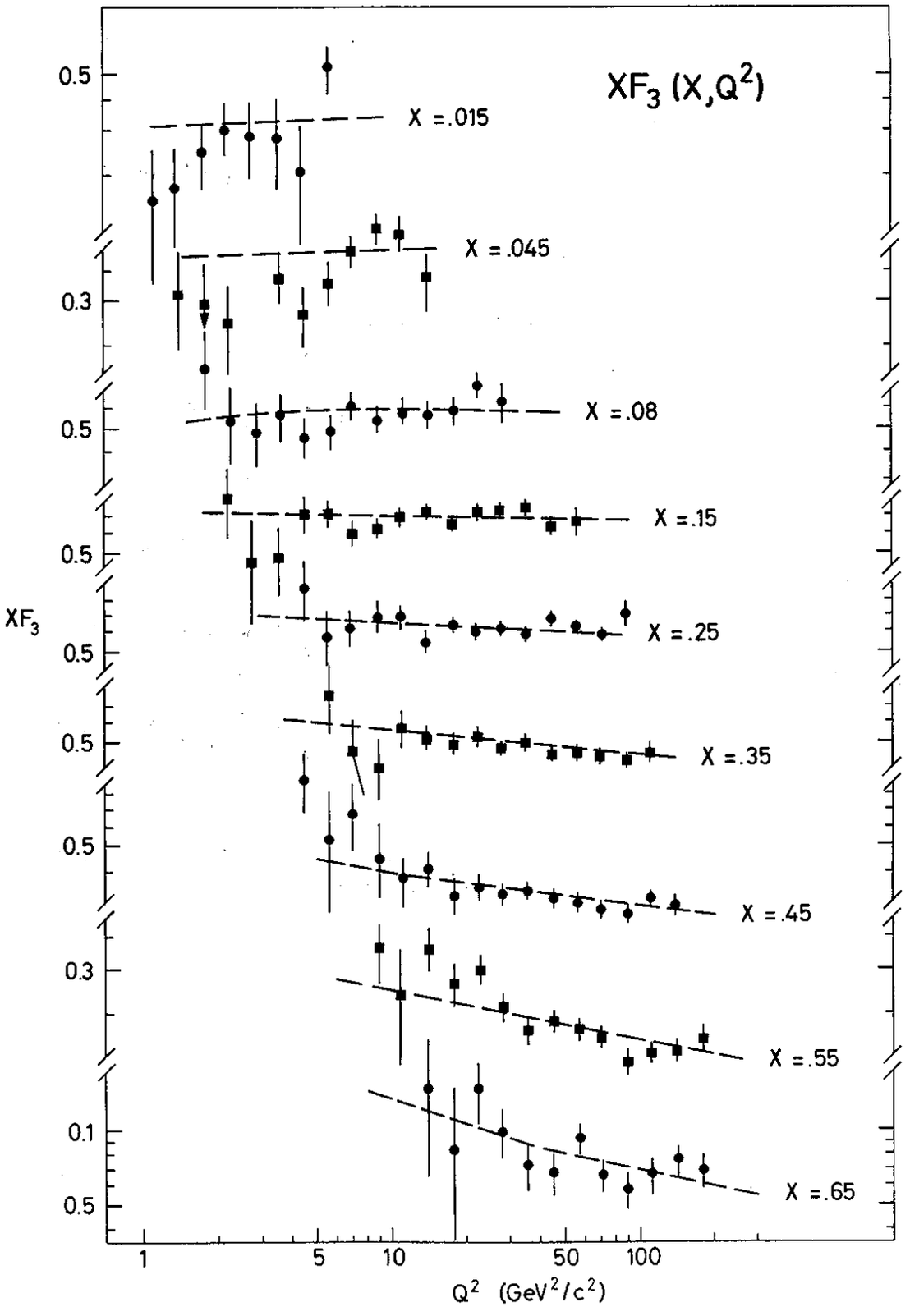
$XF_3\ (X,Q^2)$
X =.015
X =.045
X =.08
X =.15
X =.25
X =.35
X =.45
X =.55
X =.65
XF_3
0.5
0.3
0.5
0.5
0.5
0.5
0.5
0.3
0.1
0.5
1
5
10
50
100
Q^2 (GeV^2/c^2)

Fig. 11

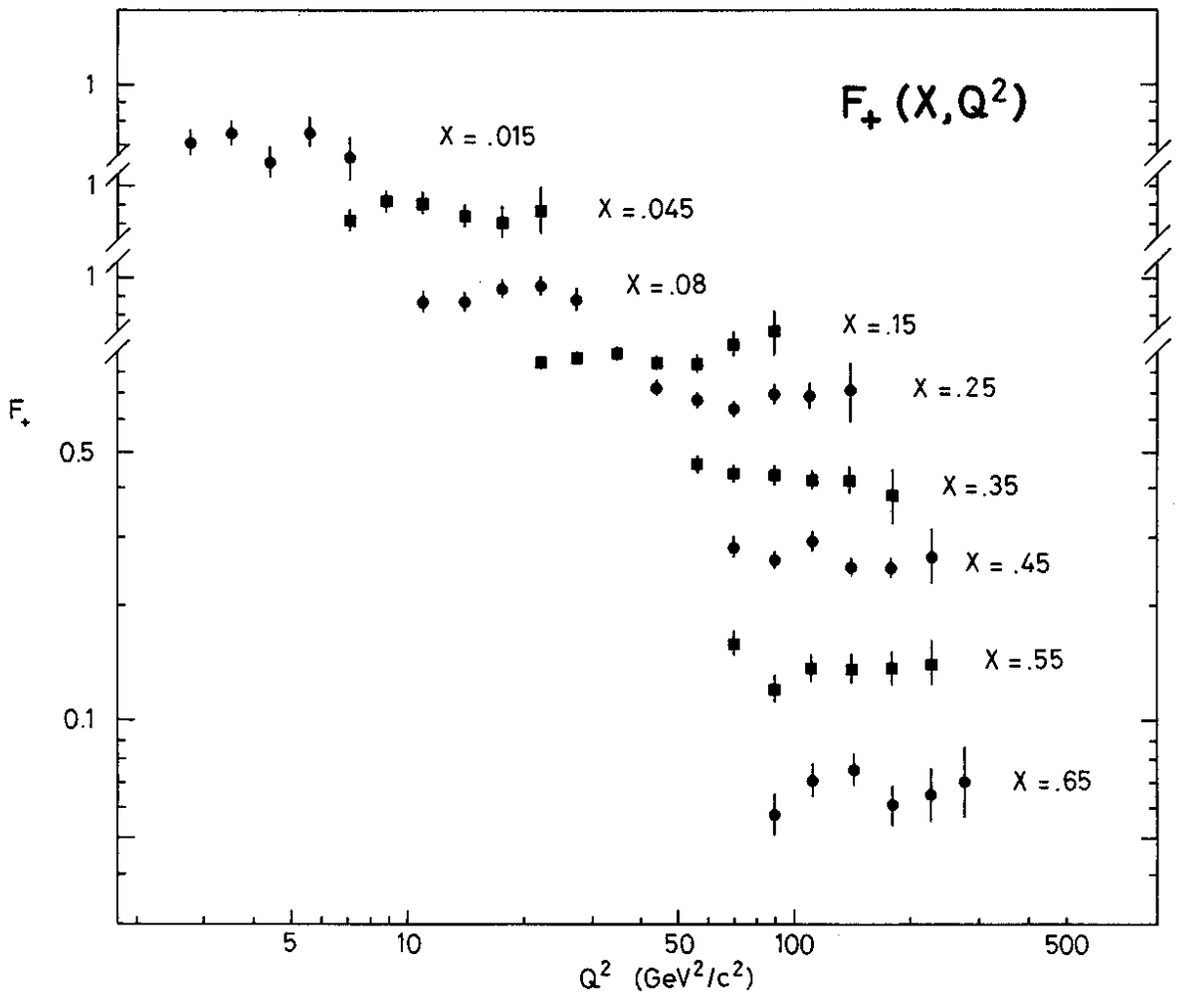
$F_+(X,Q^2)$
X = .015
X = .045
X = .08
X = .15
X = .25
X = .35
X = .45
X = .55
X = .65
F_+
1
1
1
0.5
0.1
5
10
50
100
500
Q^2 (GeV^2/c^2)

Fig. 12

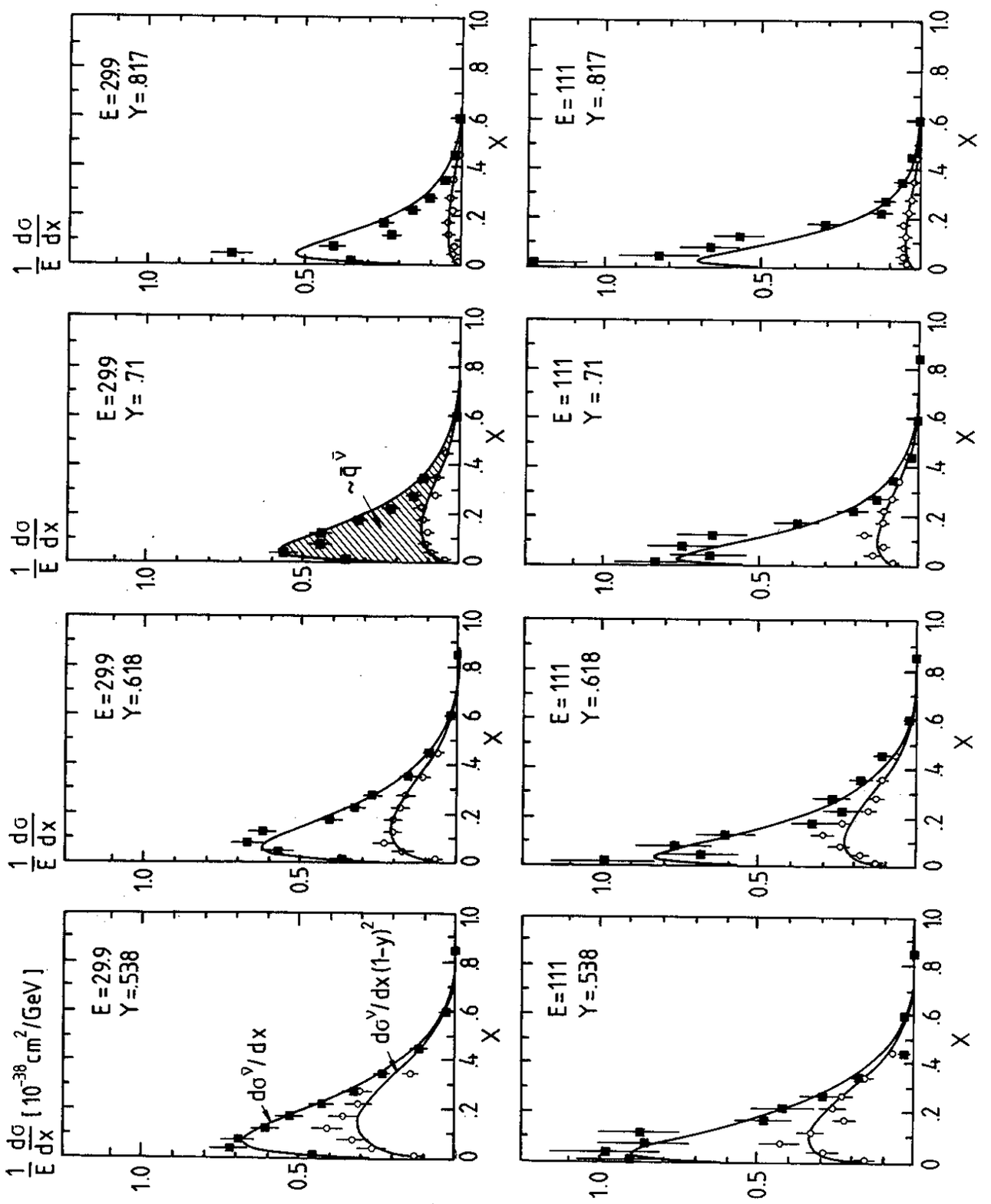
1/E dσ/dx [10^-38 cm^2/GeV]
E=29.9 Y=.538
E=29.9 Y=.618
E=29.9 Y=.71
E=29.9 Y=.817
E=111 Y=.538
E=111 Y=.618
E=111 Y=.71
E=111 Y=.817
dσ^ν/dx
dσ^ν̄/dx(1-y)^2
~q̄^ν̄
X

Fig. 13

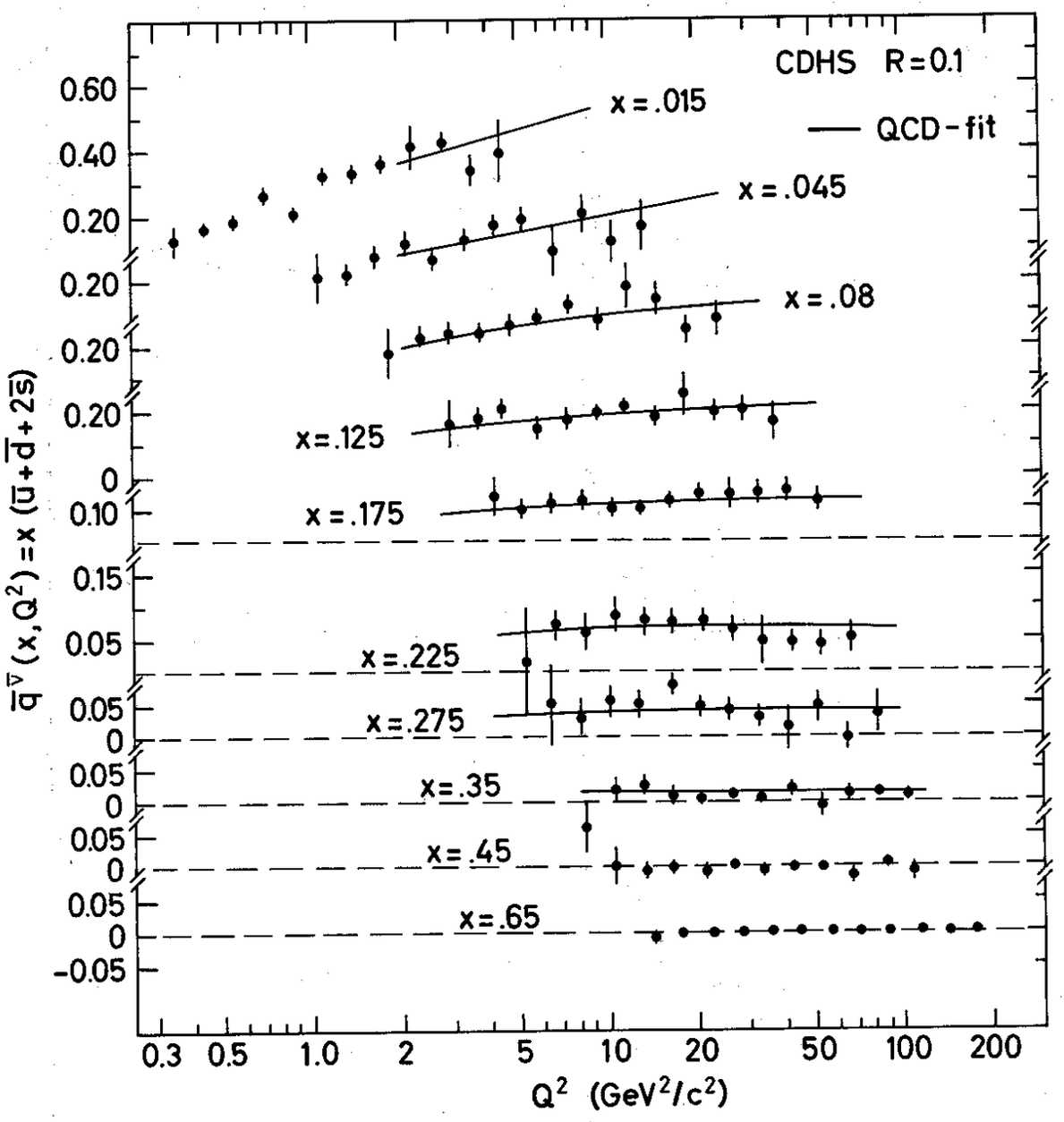
CDHS R=0.1
QCD-fit
x=.015
x=.045
x=.08
x=.125
x=.175
x=.225
x=.275
x=.35
x=.45
x=.65
$\overline{q}^{\nu}(x,Q^2)=x(\overline{u}+\overline{d}+2\overline{s})$
Q^2 (GeV^2/c^2)

Fig. 14

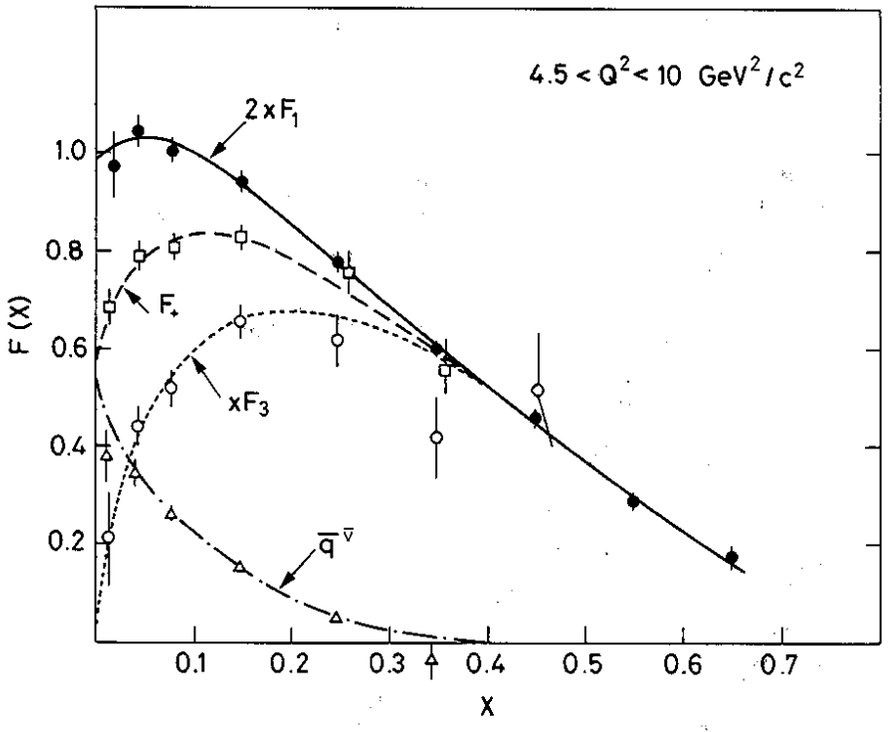
4.5 < Q² < 10 GeV²/c²
2xF1
F+
xF3
q̄ν̄
F (X)
X
1.0
0.8
0.6
0.4
0.2
0.1
0.2
0.3
0.4
0.5
0.6
0.7

Fig. 15

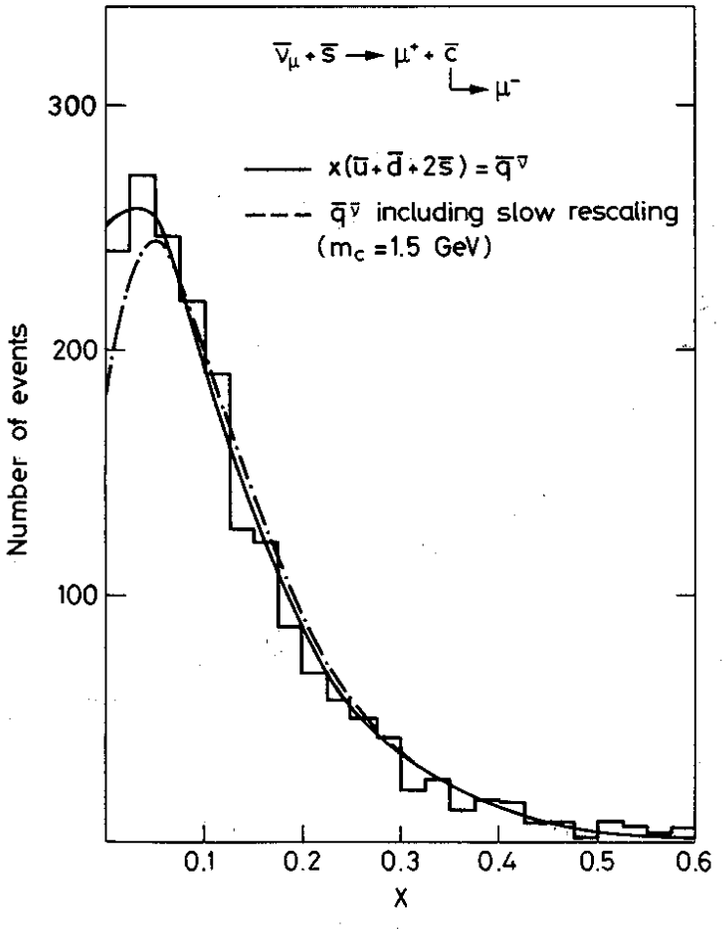
ν̄μ + s̄ → μ⁺ + c̄
↳ μ⁻
x(ū + d̄ + 2s̄) = q̄ν̄
q̄ν̄ including slow rescaling
(mc = 1.5 GeV)
Number of events
X
300
200
100
0.1
0.2
0.3
0.4
0.5
0.6

Fig. 16

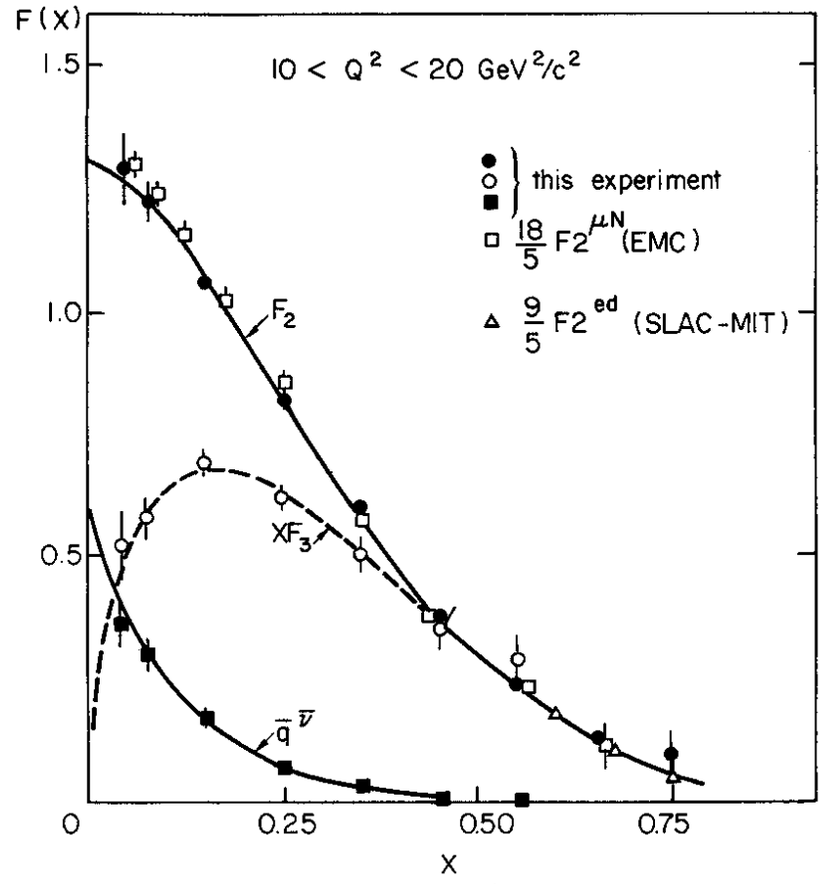
a)
F(X)
1.5
1.0
0.5
0
0.25
0.50
0.75
X
10 < Q² < 20 GeV²/c²
this experiment
18/5 F2^μN (EMC)
9/5 F2^ed (SLAC-MIT)
F2
XF3
q̄ ν̄

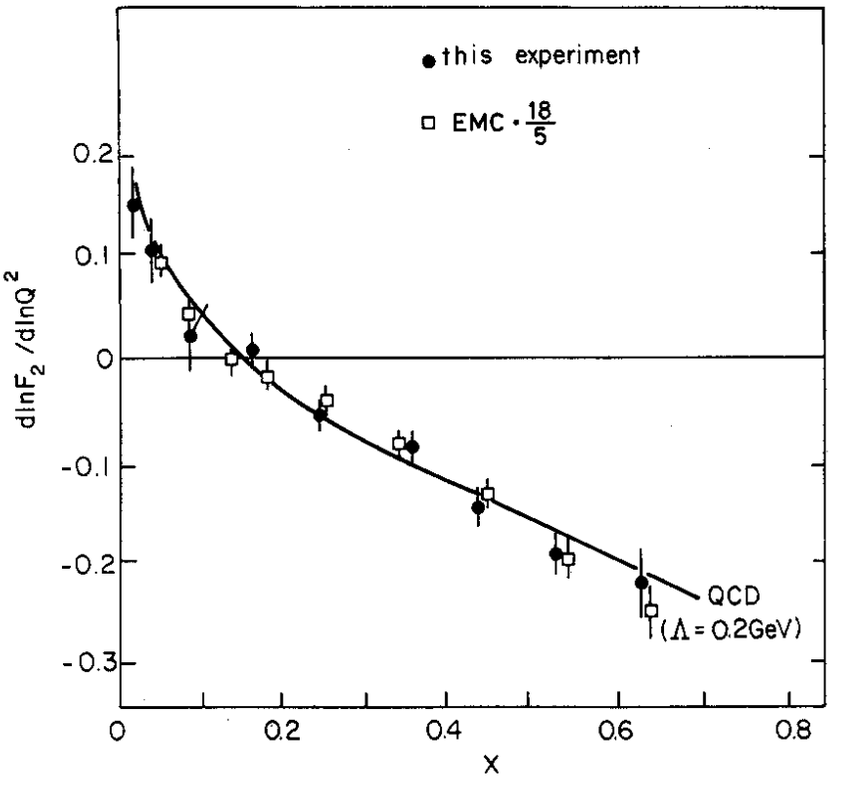
b)
this experiment
EMC · 18/5
0.2
0.1
0
-0.1
-0.2
-0.3
dlnF2 /dlnQ²
0
0.2
0.4
0.6
0.8
X
QCD
(Λ = 0.2GeV)

Fig. 17

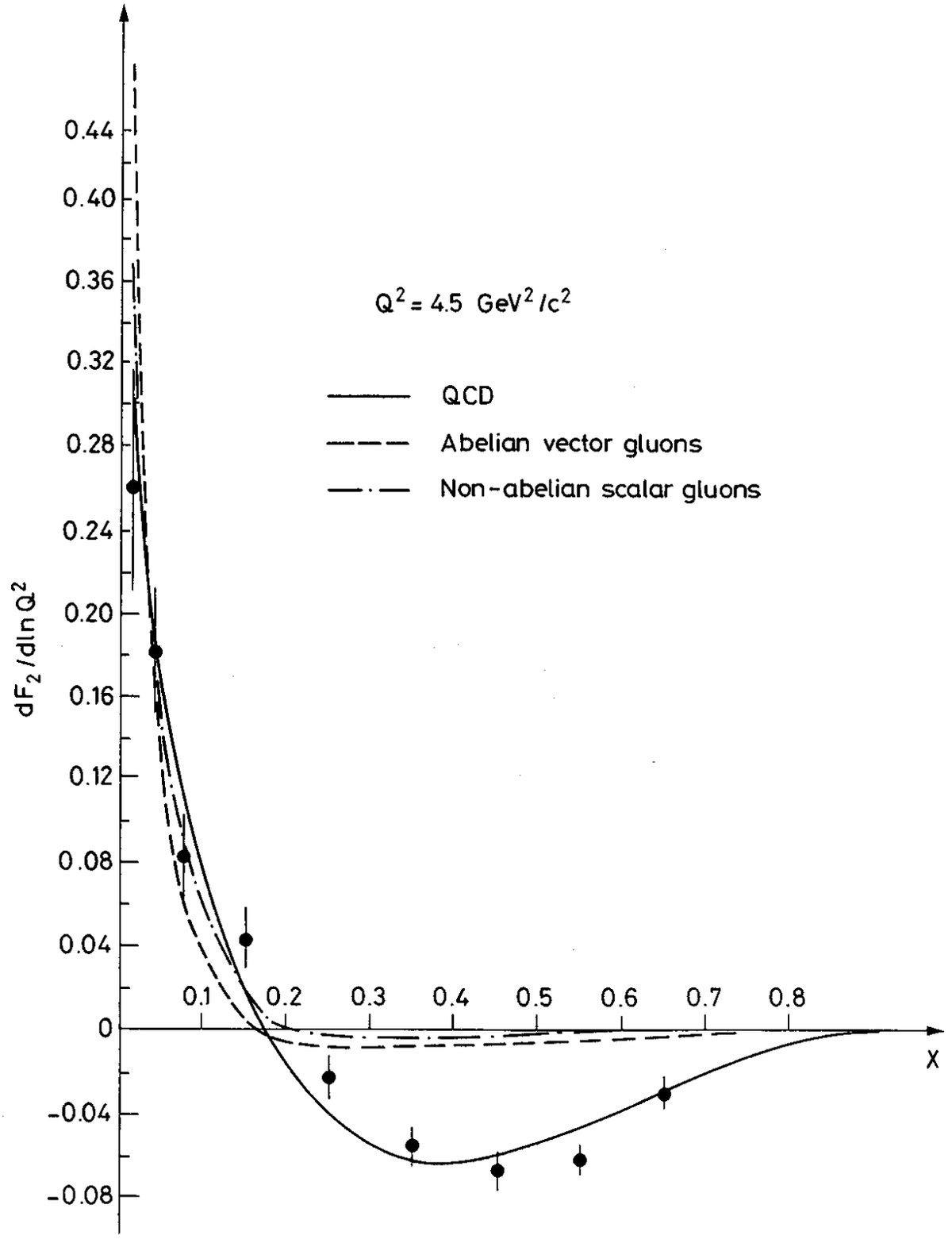
0.44
0.40
0.36
0.32
0.28
0.24
0.20
0.16
0.12
0.08
0.04
0
-0.04
-0.08
$dF_2/d\ln Q^2$
$Q^2 = 4.5\ GeV^2/c^2$
QCD
Abelian vector gluons
Non-abelian scalar gluons
0.1
0.2
0.3
0.4
0.5
0.6
0.7
0.8
X

Fig. 18 a)

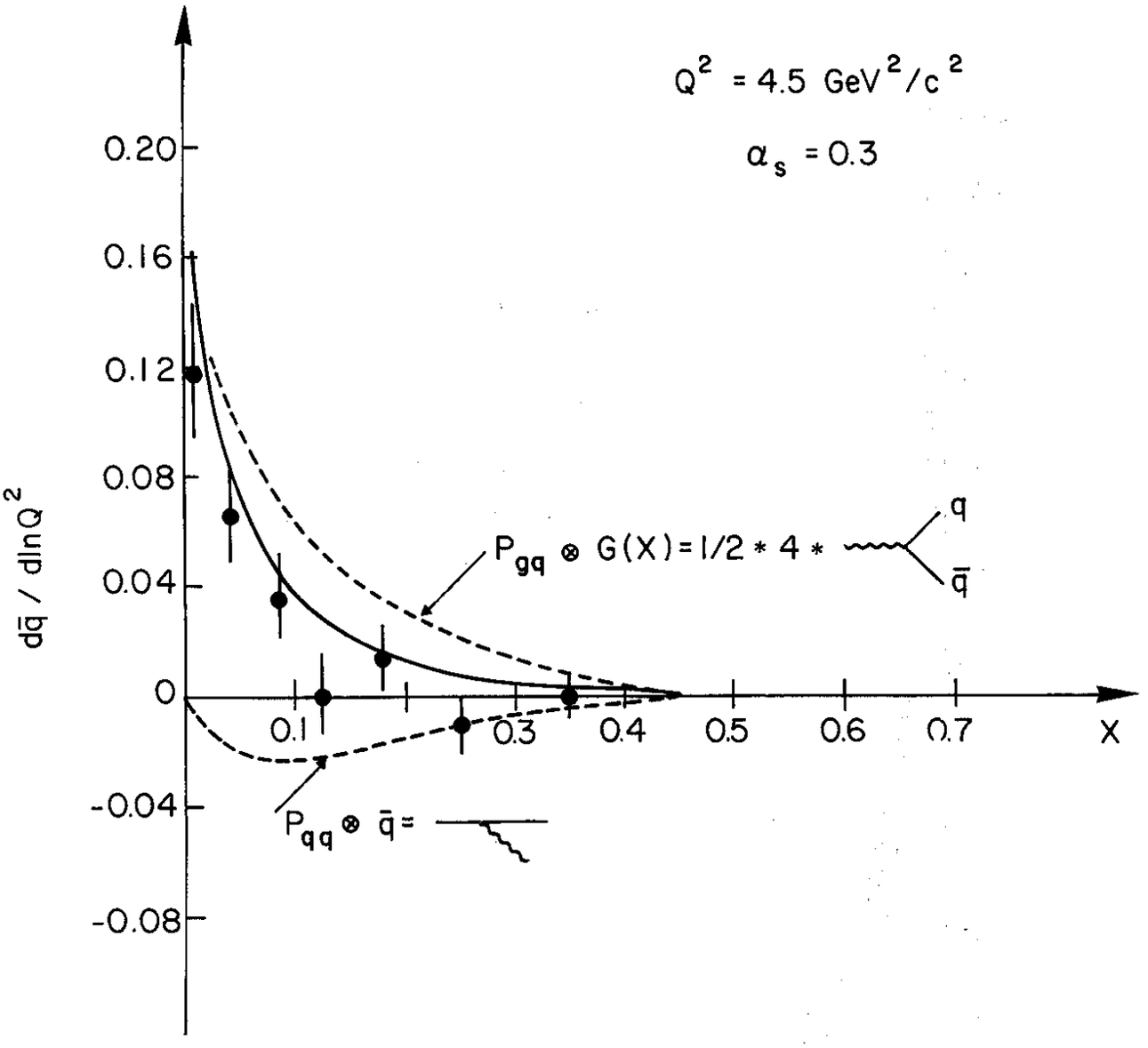
$Q^2 = 4.5\ GeV^2/c^2$
$\alpha_s = 0.3$
0.20
0.16
0.12
0.08
0.04
0
-0.04
-0.08
0.1
0.3
0.4
0.5
0.6
0.7
X
$d\bar{q} / d\ln Q^2$
$P_{gq} \otimes G(X) = 1/2 * 4 *$
q
$\bar{q}$
$P_{qq} \otimes \bar{q} =$

Fig. 18 b)

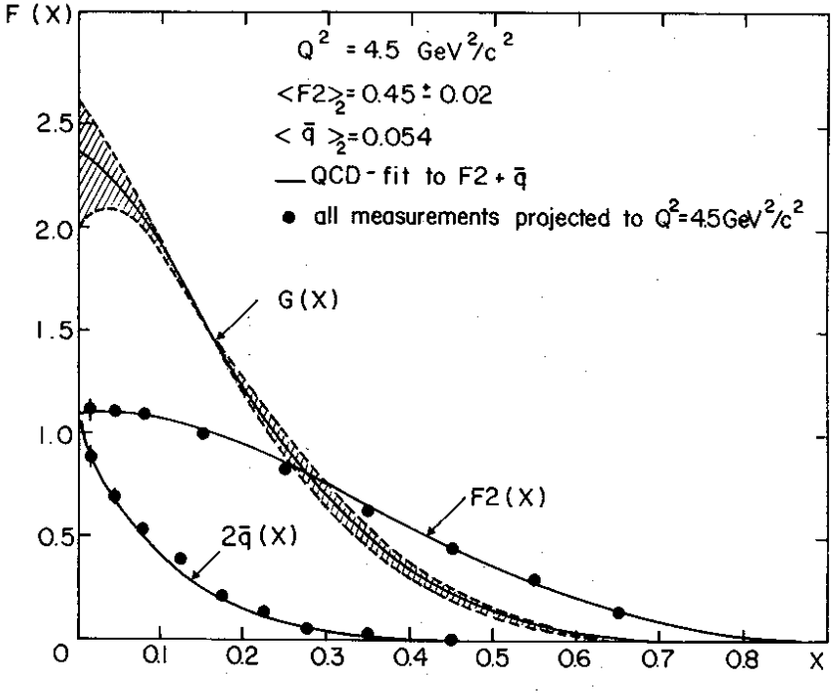
F (X)
Q^2 = 4.5 GeV^2/c^2
<F2>$_2$= 0.45 ± 0.02
< $\bar{q}$ >$_2$=0.054
QCD - fit to F2 + $\bar{q}$
all measurements projected to Q^2=4.5GeV^2/c^2
G(X)
F2(X)
2$\bar{q}$(X)
2.5
2.0
1.5
1.0
0.5
0
0.1
0.2
0.3
0.4
0.5
0.6
0.7
0.8
X

Fig. 19

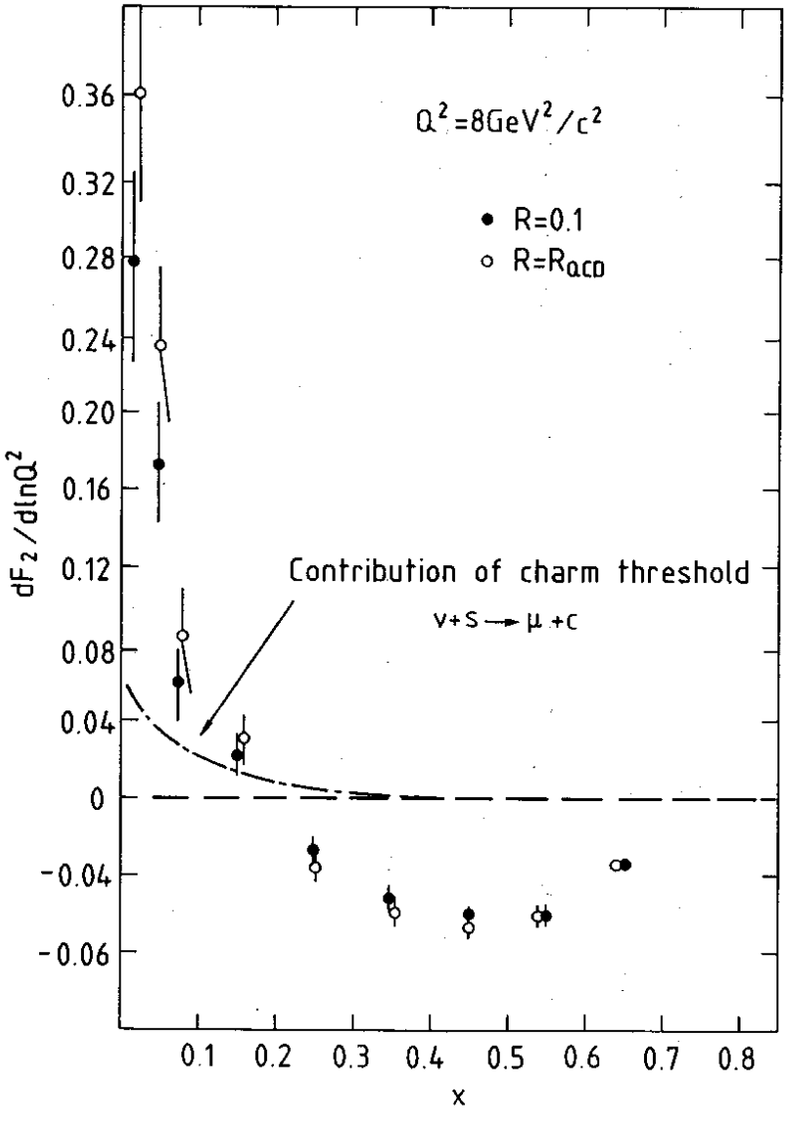
Q^2=8GeV^2/c^2
R=0.1
R=R_{QCD}
Contribution of charm threshold
ν+S → μ +c
$dF_2/d\ln Q^2$
0.36
0.32
0.28
0.24
0.20
0.16
0.12
0.08
0.04
0
-0.04
-0.06
0.1
0.2
0.3
0.4
0.5
0.6
0.7
0.8
X

Fig. 20

APPENDIX

In the following we summarize the formulae and assumptions which have been used to determine the structure functions from the measured differential cross-sections.

1) Correction of the differential cross-sections for the excess of neutrons in iron (isoscalar correction)

The correction is evaluated in the framework of the quark parton model assuming $\bar{u} = \bar{d}$. The cross-sections per nucleon in iron are given by the expressions:

$$\left.\frac{d^2\sigma^{\nu N}}{dxdy}\right|_{iron} = \left.\frac{d^2\sigma^{\nu N}}{dxdy}\right|_{I=0} + \frac{N-Z}{N+Z}\, x\left[u_v - d_v\right]\, \frac{G^2 m_N E_\nu}{\pi} \qquad (A1)$$

$$\left.\frac{d^2\sigma^{\bar{\nu} N}}{dxdy}\right|_{iron} = \left.\frac{d^2\sigma^{\bar{\nu} N}}{dxdy}\right|_{I=0} - \frac{N-Z}{N+Z}\, x\left[u_v - d_v\right](1-y)^2\, \frac{G^2 m_N E_\nu}{\pi} \qquad (A2)$$

Here Z and N are the number of protons and neutrons in iron, respectively, and the effects of the longitudinal structure function has been neglected.

The second term on the right-hand side of Eqs. (A1) and (A2) are the isoscalar corrections. They are evaluated using

$$x(u_v - d_v) = \frac{1 - d_v/u_v}{1 + d_v/u_v}\, xF_3 \ , \qquad (A3)$$

where xF_3 is the valence quark distribution as measured in the present experiment. To evaluate the structure functions F_2, xF_3, F_+, $\bar{q}^{\bar{\nu}}$, and $R = \sigma_L/\sigma_T$, we have used the simple assumption $d_v/u_v = 0.5$ such that $\left[(N-Z)/(N+Z)\right] x(u_v - d_v) = \delta x F_3$ with $\delta = (N-Z)/3(N+Z) \simeq 0.023$. The corrections are generally so small that this approximation is adequate. The evaluation of the upper limit on R in Section 4.2.1, however, is more sensitive to small corrections. For this determination we used $d_v/u_v = 0.57\ (1-x)$ which we have obtained from a comparison of neutrino and anti-neutrino interactions in hydrogen [30].

2) Relations between structure functions and differential cross-section for isoscalar targets

The structure functions have been evaluated from the differential cross-sections using the following equations:

$$\frac{\pi}{G^2 m_N E_\nu}\frac{d^2(\sigma^\nu+\sigma^{\bar\nu})}{dxdy} = F_2\left[1+(1-y)^2-y^2\left(R(1+Q^2/\nu^2)/(1+R)-Q^2/2\nu^2\right)\right] + 2x(s-c)\left[1-(1-y)^2\right] \quad (A4)$$

$$\frac{\pi}{G^2 m_N E_\nu}\frac{d^2(\sigma^\nu-\sigma^{\bar\nu})}{dxdy} = xF_3\left[1-(1-y)^2\right] \quad (A5)$$

$$\frac{\pi}{G^2 m_N E_\nu}\left[\frac{d^2\sigma^{\bar\nu}}{dxdy} - \frac{d^2\sigma^\nu}{dxdy}(1-y)^2\right] = \frac{1}{2}\left[2xF_1-xF_3+2x(s-c)\right]\left[1-(1-y)^4\right] + (F_2-2xF_1)\left[(1-y)-(1-y)^3\right] - \frac{Q^2}{4\nu^2}F_2(2y^3-y^4) - 2x(s-c)\left[(1-y^2)-(1-y)^4\right] . \quad (A6)$$

Equation (A6) is used to determine the antiquark distribution which is defined by

$$\frac{1}{2}\left[2xF_1-xF_3+2x(s-c)\right] = \bar q^{\bar\nu} + \frac{Q^2}{4\nu^2}xF_3 . \quad (A7)$$

This definition ensures that $\bar q^{\bar\nu}$ is always larger than or equal to zero owing to the inequality $2xF_1 \geq \sqrt{1+(Q^2/\nu^2)}\,xF_3$ [2].

The upper limit on $R = \sigma_L/\sigma_T$ from Section (4.2.1) is obtained from the experimental quantity:

$$\left[\frac{(d^2\sigma^{\bar\nu}/dxdy) - (1-y)^2(d^2\sigma^\nu/dxdy)}{(d^2\sigma^\nu/dxdy) - (1-y)^2(d^2\sigma^{\bar\nu}/dxdy)}\right] \geq \frac{\left[(1-y)-(1-y)^3\right]\left[R-(Q^2/2\nu^2\right]}{1+\left[(1-y)-(1-y)^3\right](Q^2/2\nu^2)} . \quad (A8)$$

The right-hand side has been obtained from equations (A6) and (A7) putting $\bar q^{\bar\nu}$ equal to zero.

Assumptions that enter into the structure function evaluation

The structure functions F_2, $2xF_1$, and $\bar q^{\bar\nu}$ can only be obtained with assumptions about $R = \sigma_L/\sigma_T$ and the difference between strange and charmed sea.

To get the values of Tables 4 and 5, we used R = 0.1 and $x(s-c) = 0.4\ x(\bar{u}+\bar{d})$ as explained in Section 4.2.5. Other assumptions can easily be applied using the correction columns of Tables 4 and 5a and Table 6.